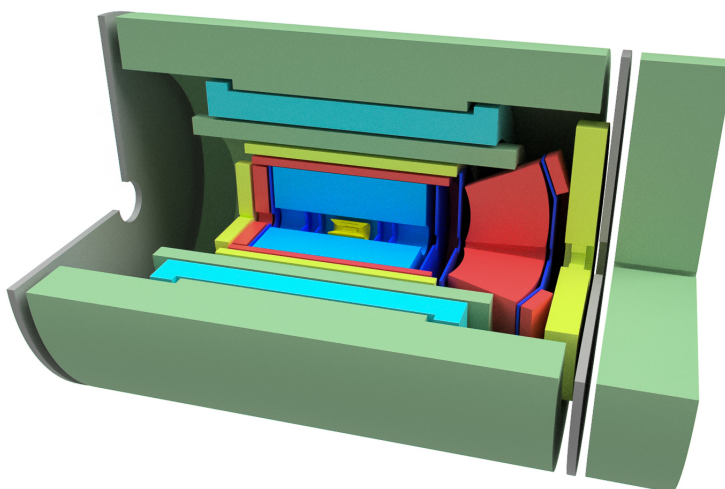# An EIC Detector Based On sPHENIX

A Letter Of Intent

(List of significant contributors)

For the EIC Detector Study Group
and the sPHENIX Collaboration
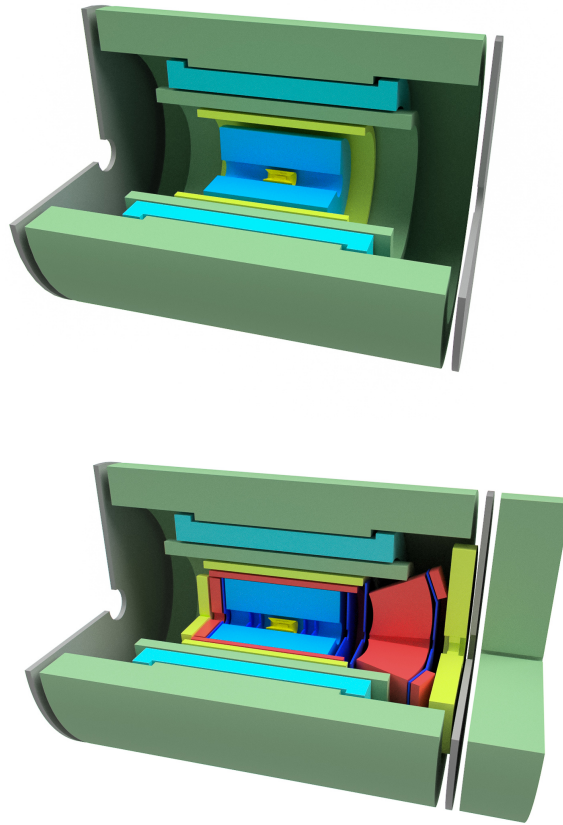
September 2018

Executive Summary

Figure 1: A 3-D rendering of sPHENIX (top) and the EIC detector based on sPHENIX described in this document (bottom).

Contents

1. The Electron-Ion Collider EIC

The Electron-Ion Collider (EIC) will be the world's first facility to collide spin-polarized electrons with polarized protons, polarized light ions, and unpolarized heavy ions at high luminosity. Using nucleons and nuclei as a QCD laboratory, it will allow for precision measurements to dramatically advance our understanding of how QCD gives rise to protons and forms nuclear matter.

After briefly introducing eRHIC as one of the proposed realizations of the EIC, this chapter outlines selected EIC measurements which are representative of the expected physics program for a general purpose detector in the first five years of eRHIC operation. Table 1.1 summarizes the measurements, the beam types being used, and the final state particles and event features that need to be detected. For a more thorough description of these measurements and the broader EIC physics program, see [1], [2], and [3].

Table 1.1: Representative EIC Measurements

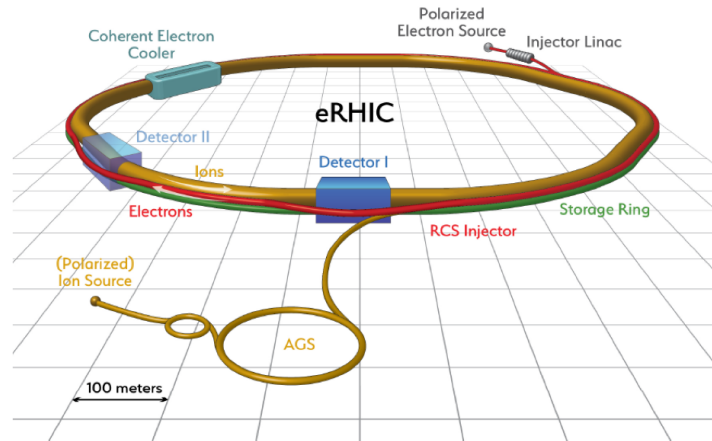| Section	Measurement	Beam	Measured Final State
1.2.1	Inclusive DIS	e+p	scattered e^-
1.2.2	Semi-Inclusive DIS	e+p	scattered e^-
			identified hadron
1.2.3	DVCS	e+p	scattered e^-
			photon
			scattered p
1.2.3	DVMP with J/Ψ	e+p	scattered e^-
			$e^- + e^+$ from J/Ψ decay
			scattered p
1.2.4	Diffraction	e+A	scattered e^-
			rapidity gap
			scattered A

Figure 1.1: eRHIC as outlined in the pre-conceptual design report [4].

1.1 Realizing EIC as eRHIC

One of the proposed realizations of the EIC, the eRHIC at BNL, plans to utilize the existing RHIC storage rings (spin-polarized protons, polarized light ions, and unpolarized heavy ions) and a high-intensity polarized electron facility to be built in the RHIC tunnel. Figure 1.1 illustrates the design. For this document, we assume the eRHIC design from the pre-conceptual design report [4] with these properties:

- up to 18 GeV electron beam energy,
- up to 275 GeV protons beam energy,
- up to 100 GeV/nucleon ion beam energy (for ions up to uranium),
- $10\ fb^{-1}$ integrated luminosity is for any given beam configuration,
- 70% polarization for both electron and proton beams,
- 22 mrad crossing angle, and
- lead (Pb) as heavy ion species, copper (Cu) as intermediate ion species, and deuterium (d) as light ion species.

We use the beam configurations listed in table 1.2. Figure 1.2 illustrates the $x - Q^2$ kinematics range for polarized electron-proton collisions reached by such an EIC and how it significantly extends the reach of existing spin-polarized data.

Table 1.2: eRHIC beam energy configurations used for this document

Colliding beams	Energy configurations (GeV x GeV)
$e+p$	8 x 275, 10 x 275, 10 x 100, 5 x 100
$e+A$	18 x 100, 10 x 100, 5 x 100

1.2 Key Measurements

1.2.1 The Longitudinal Spin of the Proton

Measuring Inclusive Deep Inelastic Scattering (DIS) in polarized electron-proton collisions at the eRHIC allows to constrain the gluon contribution to the proton spin at much lower
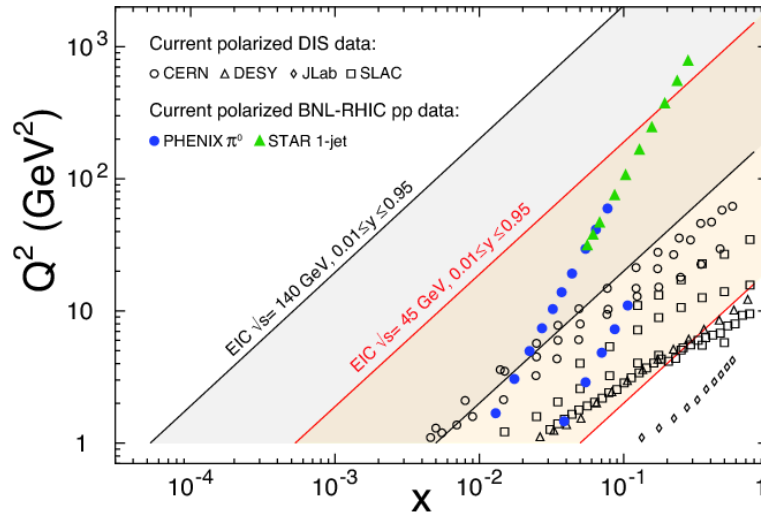
Figure 1.2: Kinematics coverage in longitudinal momentum fraction (*x*) and four-momentum transfer squared (Q^2) for polarized electron-proton collisions at the EIC [2].

values of the longitudinal momentum fraction *x* than current and other planned experiments could access. This constraint is a crucial step towards resolving the origin of the overall proton spin. Measurements from fixed target polarized DIS have determined the quark contribution, but are less sensitive to the gluon due to the small kinematic coverage. Current RHIC measurements indicate that the gluon spin contribution may be comparable or even larger than the quark spin contribution, but due to the limited coverage at low *x*, large uncertainty remains. Figure 1.3 (yellow band) shows this. The measurement requires detection of the scattered electron in polarized electron-proton collisions.

1.2.2 The Transverse Motion of Quarks and Gluons Inside the Proton

Measuring Semi-Inclusive Deep Inelastic Scattering (SIDIS) in polarized electron-proton collisions at the EIC probes the intrinsic transverse momentum distribution of quarks inside a proton. This gives a 2+1 dimensional description of the spin and momentum distributions of different quark flavors in the proton, such as shown in Figure 1.4. The kinematics range accessible at the eRHIC will extend these kinds of measurements from the valence quark regime accessible by current experiments to the sea quarks. The measurement requires detection of the scattered electron and an identified final state pion or kaon in polarized electron-proton collisions.

1.2.3 The Spatial Distribution of Quarks and Gluons Inside the Proton

Deeply Virtual Compton Scattering (DVCS) and Deeply Virtual Vector Meson Production (DVMP) are hard exclusive processes in electron-proton collisions. They involve interactions between the virtual photon and the partons in the proton without breaking the proton. DVCS results in the production of a real photon, while DVMP yields a real vector meson in the final state. Such processes probe the transverse distribution of quarks, anti-quarks, and gluons inside the nucleon, providing a 2+1 dimensional image of the
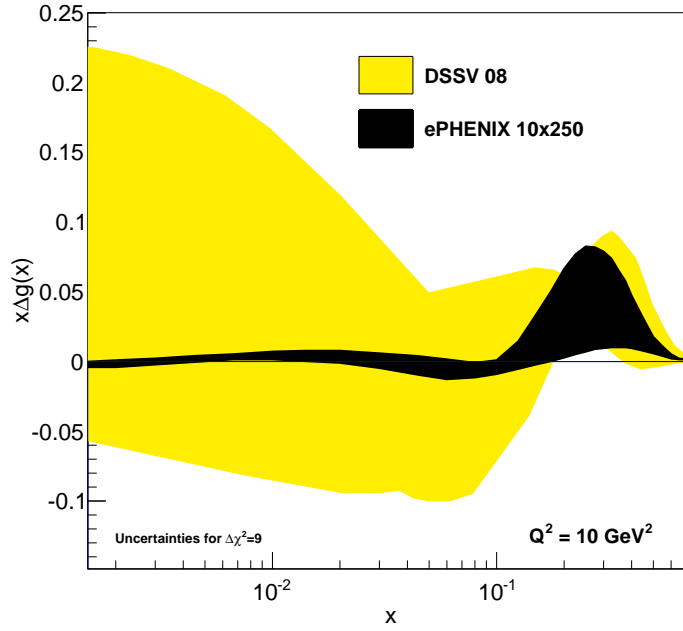
Figure 1.3: The projected reduction in the uncertainty (black) on the gluon longitudinal spin distribution based on simulated PYTHIA events corresponding to an integrated EIC luminosity of 10 fb^{-1} at 10 GeV $\times$ 250 GeV beam energy configuration [1].
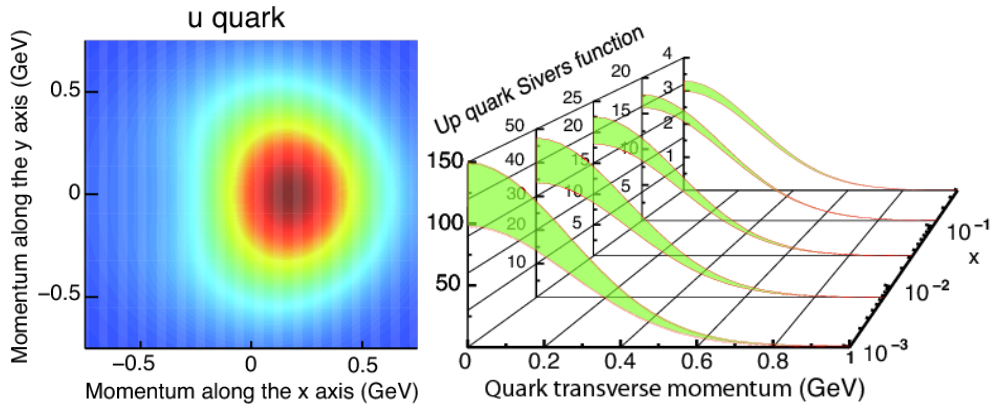
Figure 1.4: (left) The transverse-momentum distribution of an up quark with longitudinal momentum fraction $x = 0.1$ in a transversely polarized proton moving in the z-direction, while polarized in the y-direction. The color code indicates the probability of finding the up quarks. (right) The transverse-momentum profile of the up quark Sivers function at five x values accessible with the kinematics available at eRHIC, and corresponding statistical uncertainties [2].

Figure 1.5: Projected uncertainties for DVCS cross section as function of $|t|$ measurements at EIC (top) and impact parameter b_T distribution extracted from these (bottom) [2].

partonic structure of the nucleon. A Fourier transformation relates the the measured squared momentum transfer t to the proton to the impact parameter b_T. Figure 1.5 shows a projection for a DVCS and impact parameter measurement at EIC.

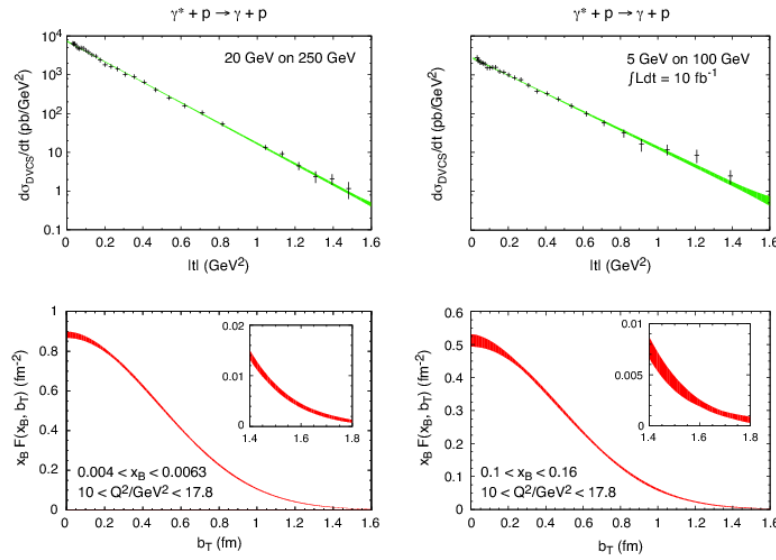The high precision data provided at EIC over a wide range of x, Q^2, and t will significantly extend the limited coverage of existing data from fixed target experiments. Therefore, they will revolutionize our capabilities to image the inside structure of nucleons. Similar measurements performed with ion beams will allow analogous imaging of nuclei.

Measuring DVCS requires detection of the scattered electron, the final state photon, and the scattered proton in polarized electron-proton collisions. Measuring DVMP requires the detection of the scattered electron, the final state vector meson (or its decay products, like e.g. electron and positron in case of J/Ψ production), and the scattered proton in polarized electron-proton collisions.

1.2.4 Gluon Saturation in Nuclei

Exploring gluonic matter at low x at the eRHIC is expected to show signs of the saturation of the density of gluons as the rate of gluon recombination balances that of gluon splitting. An experiment at eRHIC is in an excellent position to map this physics out in the gluon sector. Figure 1.6 shows the x and Q^2 coverage of a detector at eRHIC for the 10 GeV $\times$ 100 GeV/nucleon configuration and the region where such an experiment can effectively search for saturation effects.

It can be particularly effective to explore this region of dense gluonic matter with diffractive physics, where at least two gluons are exchanged in the interaction. Therefore, a primary measurement to probe saturation effects at eRHIC will be comparing the diffractive-to-total cross-section from $e+p$ and $e+$A. The ratio of these cross-sections will directly relate to the size of any saturation effects.

Measuring diffractive events requires wide calorimetric coverage to clearly identify
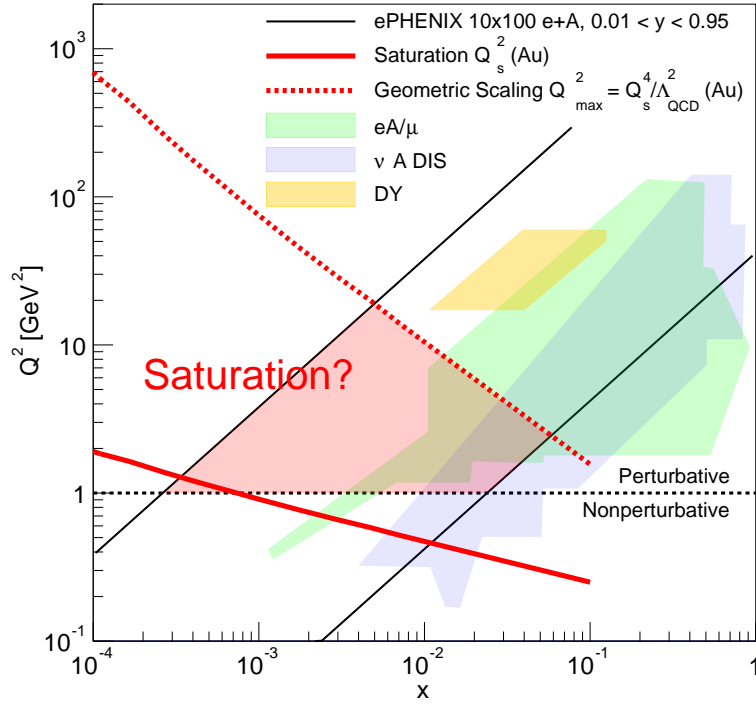
Figure 1.6: The kinematics coverage in x and Q^2 for collisions of 10 GeV electrons on 100 GeV/nucleon ions at eRHIC and the kinematic coverage of previous e+A and ν+A DIS and Drell-Yan experiments. The area between the solid and dashed red lines indicates the range from the saturation scale Q_s^2 to $Q_{max}^2 = Q_s^4/\Lambda_{QCD}^2$ according to geometric scaling [1].

1   large rapidity gaps. These gaps are a characteristic feature of diffractive events, because
2   the hadron remains intact after the scattering.

2. Detector Concept

The sPHENIX detector forms a suitable basis for an experiment at a future Electron Ion Collider (EIC, [2]). An EIC detector based on sPHENIX has excellent performance for a broad range of EIC physics measurements.

Figure 2.1 illustrates the design of an EIC detector based on sPHENIX that utilizes the sPHENIX superconducting solenoid, barrel tracking, and barrel calorimetry. In addition, this design foresees a GEM tracking station, an aerogel RICH, and a crystal calorimeter at negative pseudorapidities to provide electron and photon identification and separation with high resolution. Moreover, it includes a barrel DIRC ('Detection of Internally Reflected Čerenkov light') in the central rapidity region. The positive pseudorapidity range will be upgraded with GEM tracking stations and an electromagnetic and hadronic calorimeter. A combination of a gas RICH and an aerogel RICH at positive pseudorapidities completes the mandatory particle identification coverage. All of these PID detector technologies are currently being studied by the EIC detector R&D consortia eRD6 and eRD14. One of these technologies is an aerogel RICH detector called mRICH for its modular and compact design. Finally, this EIC detector will require Roman Pot detectors in the very forward region to detect the scattered beam proton in exclusive deep inelastic scattering events. The detector configuration studied in this document is summarized in Table 2.1.

Section 2.1 discusses the planned reuse and modification of sPHENIX components. The following sections discuss the current design for an EIC detector based on sPHENIX in more detail.

2.1 Use of sPHENIX components

Using sPHENIX as a basis for an EIC detector allows to capitalize on the the investment made into sPHENIX for an EIC detector. This is a list of sPHENIX components that can be reused:
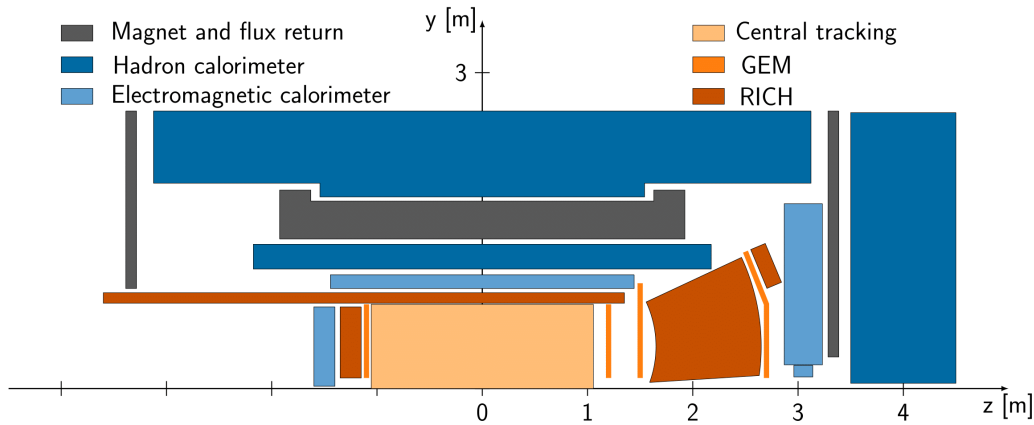
- Magnet.
- Barrel Flux Return.

Figure 2.1: Design of an EIC detector based on sPHENIX that uses the sPHENIX superconducting solenoid, barrel and forward tracking, and barrel and forward calorimetry. It adds tracking and calorimetry at negative pseudorapidities, as well as RICH detectors for PID at central, negative, and positive pseudorapidities.

- Endcap Flux Return Door on electron-going side.
- Outer HCAL scintillator.
- TPC. Replace inner 1/3 sector endcaps to extend instrumentation towards the inner field cage. Reason: space charge not as large an issue, so additional path length can be used for tracking.
- TPC Electronics. Statement is that TPC dE/dx resolution can be recovered by different working point without modifications.
- Data Acquisition. At 1034 can handle full minbias event rate. However, investigation needed on rejection of the 10 MHz beam-gas rate.
- Detector infrastructure in BNL experimental hall 1008. Racks, computers, etc.

sPHENIX components that need to be removed or replaced:

- Endcap Flux Return Door on hadron-going side needs to be removed; use magnetic HCAL in that direction as flux return.
- INTT - will not be reused.
- MVTX - cannot be reused, because of larger radius of the beam pipe and need to extend signal readout to higher z. Would need to change out both staves and mechanical structure.
- SiPMs for EMCal and HCal - likely need to be replaced.
- Electronics - EMCal and HCal electronics need to be changed to handle higher readout and bunch crossing rate.

sPHENIX components that are included in this EIC detector design with modification:

- Barrel EMCal needs to be either extended in pseudorapidity or replaced by a different calorimeter to ensure sufficient electromagnetic calorimeter coverage in pseudorapidity.
- Inner HCAL - since its primary purpose in CD-1 detector is as a holding structure for EMCal, depends on decision of EMCal reuse and engineering of modification to EMCal to extend coverage.

Table 2.1: EIC-sPHENIX Detector Coverage

Detector	pseudorapidity	Type
TPC	(-1.1, 1.1)	Tracking
TPC + MAPS + GEM	(-4, 4)	Tracking
barrel EMCAL	(-1.55, 1.242)	Calorimetry
barrel inner HCAL	(-1.1, 1.1)	Calorimetry
barrel outer HCAL	(-1.1, 1.1)	Calorimetry
e-side EMCAL	(-4, -1.55)	Calorimetry
h-side EMCAL	(1.242, 4)	Calorimetry
h-side HCAL	(1.242, 5)	Calorimetry
DIRC	(-1.24, 1.24)	PID
dRICH	(1.24, 3.95)	PID
gas RICH	(1.24, 3.95)	PID
h-side mRICH	(1.10, 1.85)	PID
e-side mRICH	(-3.9, -1.4)	PID

2.2 Calorimetry

2.2.1 Electromagnetic calorimetry

Electromagnetic calorimetry will be essential across the backward, midrapidity, and forward regions in order to measure the scattered electrons, DVCS photons and detect hadronic products such as photons from hadron decays and therefore aid to jet reconstruction. Three different electromagnetic calorimeters are envisioned for the backward, midrapidity, and forward regions.

Electron EMCal (EEMC)

The calorimeter in the electron-going direction consists of an array of lead tungstate (PbWO$_4$) crystals (commonly known as PWO), similar to the endcap crystal calorimeter designed for the PANDA experiment and shown in Figure 2.2. A similar EMCal has been built for the CMS experiment at the LHC (CERN) with energy resolution $\sigma_E/E \sim 2.8\%/\sqrt{E(GeV)}$. An enhanced light output version of lead tungstate (PWO-II) can provide higher light yield than the CMS EMCal resulting in a relative energy resolution better than $2\%/\sqrt{E(GeV)}$. The proposed PWO calorimeter for an EIC detector based around the BaBar solenoid will consist of $\sim$ 5000 crystals, and will have a similar size and shape to the PANDA crystals (with projective geometry, pointing to the nominal collision vertex). They will be $\sim$ 2 cm $\times$ 2 cm (corresponding to one R_M^2) and will be read out with four SiPMs.

Central EMCal (CEMC)

The sPHENIX CEMC is a critical component of the midrapidity implementation of an EIC detector based around the BaBar solenoid. The design of the CEMC is composed of 24,596 towers at an inner radius of approximately 90 cm with a segmentation of 0.025×0.025 in $\Delta\eta \times \Delta\phi$. This covers the full azimuth with a pseudorapidity coverage of $|\eta| < 1.1$. The CEMC has been designed to occupy minimal radial space such that it can fit within the BaBar solenoid with the central tracking detectors, while also providing moderate energy resolution at a low cost. The large solid angle coverage and additional condition of
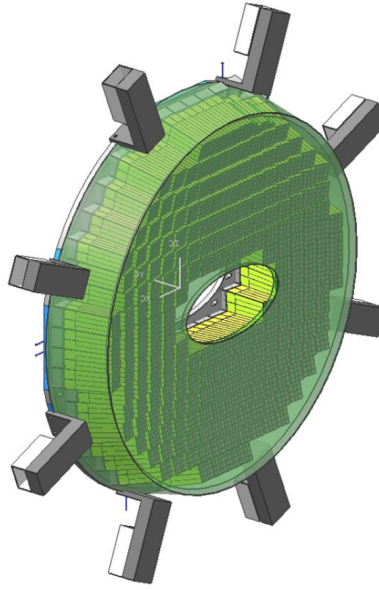
Figure 2.2: PANDA Crystal Endcap Calorimeter. The PWO crystal modules are shown in green, which is projective towards the nominal interaction point.

good uniformity are necessary for reconstructing the electromagnetic component of jets at central rapidities.

The CEMC towers are composed of a matrix of scintillating fibers embedded into an absorber consisting of a mixture of tungsten powder and epoxy. This is similar to the SPACAL design that has been used in several other experiments [5, 6]. The towers are read out via silicon photomultipliers, which provide high gain, require minimal space, and can operate within the central magnetic field. The design of the towers provides an approximately 2% sampling fraction with a total radiation length of approximately $18X_0$. The towers in the EMCal are also 1D projective for $|\eta| < 0.15$ and 2D projective for $|\eta| > 0.15$, meaning that they are tilted in azimuth or azimuth and pseudorapidity at small or large pseudorapidities, respectively. The projective towers provide a more uniform shower development, especially at large pseudorapidity, which improves both the energy resolution and scale of the calorimeter by containing the shower to approximately one tower.

In total, four separate beam tests have been performed for 1D and 2D projective prototype calorimeters. The beam tests have provided an opportunity to evaluate the specifications of the calorimeter as well as improve the tower construction process. Figure 2.3 (left) shows that the resolution of the 1D projective towers is approximately $2.8\% \oplus 15.5/\sqrt{E}\%$, as determined in the 2016 sPHENIX beam test [7]. The high rapidity projective towers in both azimuth and pseudorapidity were tested in 2017, and the measured resolution was found to be approximately $4\% \oplus 15/\sqrt{E}\%$. However, this is expected to improve as these were the first 2D projective towers ever built; another test beam with a new calorimeter that has improved uniformity was tested in early 2018 and data analysis is ongoing.
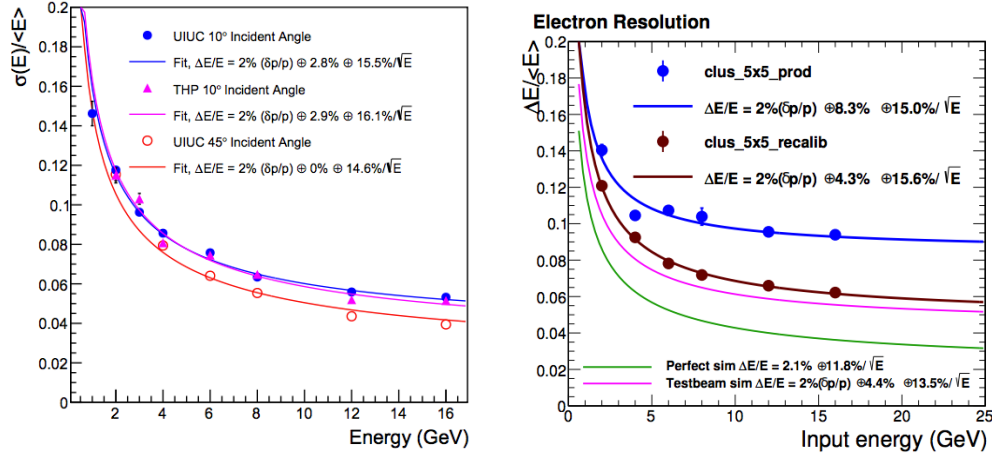
Figure 2.3: The resolution of the central rapidity towers $|\eta| < 0.15$ projective in azimuth is shown (left), as determined from a test beam performed in 2016 [7]. The resolution of the high rapidity towers $|\eta| > 0.15$ projective in azimuth and pseudorapidity is shown (right), as determined from a test beam performed in 2017 [8].

There are several aspects of the sPHENIX CEMC that need to be assessed further with regards to reuse for an EIC detector. Since the current implementation of the sPHENIX CEMC only covers $-1.1 < \eta < 1.1$, there is a gap in electromagnetic calorimetry between the EEMC and CEMC in the range $-1.4 < \eta < -1.1$. Eliminating this gap would provide better x - Q^2 coverage since it is in the electron going direction. While detailed engineering considerations have yet to be explored, there is space available in the current EIC detector design to extend the sPHENIX CEMC in the negative pseudorapidity direction to cover this gap. This extended CEMC, covering $-1.4 < \eta < 1.1$, has been implemented within the GEANT4 description of the EIC detector based around the BaBar solenoid. Additional tests are also required to determine the reusability of certain aspects of the CEMC; for example, since the readout is performed by silicon photomultipliers these may need to be replaced since they will have incurred several years of radiation damage during the sPHENIX running period.

Forward EMCal (FEMC)

For electromagnetic calorimetry in the hadron-going direction, we propose to refurbish the PHENIX lead-scintillator (PbSc) sampling calorimeter (used in the PHENIX Central Arms) with a transverse tower size of 5.5×5.5 cm^2 and an energy resolution of $\sigma_E/E \sim 8\%/\sqrt{E(GeV)}$.

A nearly circular EMCal of $\sim$170 cm radius covers the sPHENIX forward acceptance at $\sim$3 m distance from the center of the solenoid magnet. The calorimeter sits just inside the magnetic flux return. An assembly of 788 PHENIX PbSc blocks covers the pseudo-rapidity range of $1.25 < \eta < 4$. The current sPHENIX barrel HCal support ring covers the region $1.1 < \eta < 1.4$; however, our current design foresees reducing the material of this support ring and extending the CEMC from $\eta < 1.1$ to $\eta < 1.25$ to provide full EMCal coverage, in conjunction with the FEMC, in the hadron going direction. Each PHENIX PbSc calorimeter block contains four optically isolated modules arranged in

a 2×2 matrix. The modules consist of alternating lead and plastic scintillator tiles and measure $5.5{\times}5.5{\times}37.5$ cm^3, which corresponds to a depth of 18 X_0. Wavelength-shifting fibers penetrate this structure to collect light from the scintillators. In the center of every block, there is a 2 mm diameter "leaky" fiber which delivers laser light to each of the four modules to monitor their gain. The signals from each PHENIX PbSc module are recorded individually. Similar to the current sPHENIX barrel calorimeter design, we propose to use silicon photomultipliers (SiPMs) as light sensors. This would allow for developing readout electronics for the forward calorimeters that are very close to those being developed for the sPHENIX barrel calorimeters. Other advantages of choosing SiPMs are their low cost (compared to conventional photomultiplier tubes), compact design, insensitivity to low energy neutron background, and their ability to operate inside of magnetic fields. An alternative to SiPMs that is being studied are avalanche photodiodes (APDs).

Additional tests are required to confirm the viability of this calorimeter design for forward instrumentation at an EIC detector based around the BaBar solenoid, including the SiPM performance. The PHENIX PbSc calorimeter technology has proven to be robust, and 16 years of operation in PHENIX have not shown any degradation of the calorimeter characteristics. However, particle densities in the forward region with the high luminosity beams projected for 2020+ are expected to be much higher than in the PHENIX central arm acceptance. While PHENIX finished its operation in 2016, the STAR interaction region still provides a test area for different detector technologies in actual RHIC beam and background conditions. We will gratefully benefit from the ongoing studies in STAR forward region, related to PbSc calorimeter radiation hardness, SiPM stability, and neutron backgrounds.

2.2.2 Hadronic Calorimetry

Hadronic calorimetry is planned for the midrapidity and forward regions. At midrapidity, the sPHENIX Outer HCal, which additionally serves as the flux return, will be reused. It covers $-1.1 < \eta < 1.1$ [ck] and is comprised of steel and scintillating tiles. [Add slightly more detailed description.] In the forward region, a [] hadronic calorimeter is envisioned, covering $[] < \eta < 5$. The extended coverage to more forward rapidity than the FEMC will aid with [jet reconstruction all the way out to $\eta = 4$[ck], more complete detection of the hadronic final state for the purpose of using hadronic reconstruction of event kinematics, and greater hermeticity for diffractive events in which a rapidity gap is required.]

2.3 Charged particle tracking

MAPS, TPC (plus micromega layer for timing), forward and backward GEM tracking stations.

2.4 Particle identification

Excellent particle identification (PID) is an essential requirement for a future Electron-Ion Collider (EIC) detector. In particular, a sensitivity to quark flavor is much more important for the EIC than for most high-energy physics (HEP) experiments. Another aspect particular to the EIC, is that the distribution of final-state particles is very asymmetric (due to the large difference in the energies of the incoming lepton and ion beams), and that the

physics of interest requires detection and identification of particles over the full angular range. Providing this coverage despite the asymmetric collisions requires an integrated suite of detector subsystems.

The PID detector choices are mainly determined by three factors: (1) particle kinematics coverage; (2) spatial constraints; and (3) the relative cost. We closely follow the work by the EIC PID Consortium (eRD14 Collaboration) and adopt the PID detector design concept within the constraints of sPHENIX detector envelope.

For the central barrel region, we will choose a high-performance DIRC (Detection of Internally Reflected Cherenkov light) to provide K/π separation up to ~ 6 GeV/c. In the hadron-going direction, given the much higher momentum reach of the final state hadrons, we plan to use a gas RICH (kinematic coverage? $1.24 < \eta < 3.95$) and an array of modular RICH (mRICH) [ref] which covers an η-range of $1.10 < \eta < 1.85$). The mRICH can provide K/π separation in the momentum range from 3 to 10 GeV/c. In the electron-going direction, we also add an array of mRICH with the pseudorapidity coverage of $-3.9 < \eta < -1.4$ for e/π separation at lower momentum range (~ 1.5 GeV/c range).

Note: Need to see the possibility of a fast TOF detector for the barrel region as the one that Mickey has developed.

The ability to identify hadrons in the final state is a key requirement for the physics program of the EIC. Being able to tag the flavor of the struck quark in semi-inclusive DIS can, for instance, tell us something about the transverse momentum distributions (and potentially orbital angular momentum) of the sea. The quark then hadronizes into a pion or a kaon, taking essentially all of the momentum transferred from the scattered electron. In this subprocess, the kaon momenta are higher than the often-shown momentum distribution for kaon production in inclusive Deep-Inelastic Scattering (DIS), which essentially sums over all combinations of final-state hadrons for a given kinematics (x, Q^2) of the scattered electron. Here it is important to cover a wide range in meson momentum fraction (vis a vis the 'jet'). Failing to do so will restrict the kinematical reach of the EIC regardless of the beam energies provided by the accelerator. Another important case to consider is when the kaons are not produced in the primary process but are decay products of heavier mesons. An example is open charm (D-mesons), which is important for probing the distribution of gluons in protons and nuclei.

While the distribution of produced particles thus depends on the specific process, in the detector endcaps the kinematics for meson production follow the energies of the colliding beams. If the scattering produces a meson traveling in the direction of the proton (ion) beam, this meson can have a momentum which is a significant fraction of the original beam momentum. If the meson is produced in the opposite (electron) direction, it cannot acquire more momentum than that carried by the electron beam. In the central region, it is possible to produce a range of momenta, but the distribution is driven by the kinematics of the process (Q^2, p_T) rather than the energies of the colliding beams. A greater reach of the PID coverage directly translates into, for instance, a larger lever arm in Q^2 – a key goal for the EIC – as well as an ability to probe deeper into the high-pT region of semi-inclusive DIS. In both cases (high Q^2 and high p_T) the event rates are low, but the physics impact is high. The Q^2 coverage at central angles (mid rapidity) does, however, grow very quickly with particle momentum. To satisfy the physics goals of the EIC, it is thus desirable to provide K/π identification in the central barrel up to at least 5 GeV/c,

with 6˜7 GeV/c being ideal. In the electron endcap, one would need to provide hadron ID up to a significant fraction of the electron beam energy ($\sim$10 GeV/c), while in the hadron endcap one would need to reach a significant fraction of the proton or ion beam momentum ($\sim$50 GeV/c).

In the electron-going direction, it is also crucial to identify the scattered electron amid a background of negative pions. Electron identification is also important for production of particles (e.g., charmonia) which decay into leptons. Here, the main detector system is the electromagnetic (EM) calorimeter, which provide e/π separation over the full momentum range. Nevertheless, the PID systems primarily intended for hadron identification can also provide an important supplementary capability for e/π. This is particularly important at low momenta (below 2-3 GeV/c), where there is a large pion background, and the suppression provided by the EM calorimeter ($\sim$ 100:1) is not sufficient. By combining the EM calorimeter with a Cherenkov detector, this suppression factor can be increased, effectively extending the kinematic reach of the collider which can then probe deeper into the low-x region, where the scattered electron loses a lot of energy in the lab frame.

2.4.1 Barrel DIRC Detector

This detector uses total internal reflection in a very precisely machined and polished bar with high refractive index (quartz), which also acts as radiator, to collect the Cherenkov photons on a small sensor plane. And while the quartz bars are expensive, they cost much less per unit area than the cheapest photosensors. In addition, the bars are very thin (2 cm) even with support structures included (5-6 cm), making the DIRC ideal for the large barrel region of the central detector, where radial space is at a premium. The key to the performance of DIRC detectors lies in the optics projecting the photons emerging from the bar onto a focal plane, and the possibility to measure the time of propagation for the photons. The original BaBar DIRC used simple pinhole focusing, and the timing resolution was about 2 ns, which was used to remove out-of-time background hits. Relying on spatial imaging only (x,y on the focal plane), it reached 3σ K/π separation for almost 4 GeV/c. Since then the development has taken three paths. One was the addition of focusing optics, as demonstrated by the FDIRC R&D at SLAC (which uses mirror-based optics). The second is exemplified by the Belle II TOP DIRC, which relies primarily on timing and only has a limited spatial imaging capability. While the performance of the TOP is comparable to that of the original BaBar DIRC, it achieves this with a very small image expansion volume and compact readout, which was the only way to make it fit the Belle II detector, which was not originally designed for a DIRC, but decided to adopt one for the upgrade after seeing its success at BaBar. Another advantage of the TOP is that its wide radiator bars ("plates") are cheaper per unit area than those of the BaBar DIRC. The third path is to combine spatial imaging with good timing ($<$ 100 ps) to perform 3D reconstruction. The joint PANDA and EIC R&D effort has shown that this approach is feasible and promises to deliver very high performance (4σ K/π at 6 GeV/c). The configuration explored for the EIC uses newly developed advanced lenses for focusing, for a sharper ring image and significantly increased photon yield. The lens-based optics also allow for a compact expansion volume which facilitates integration with other subsystems.
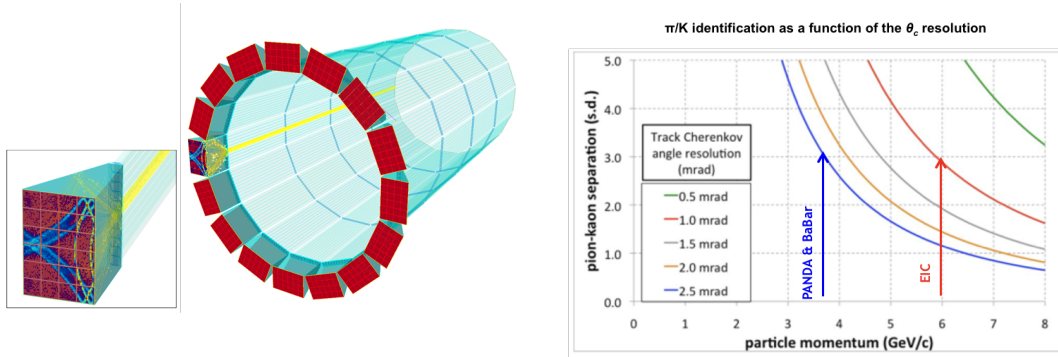
Figure 2.4: DIRC design and performance.

2.4.2 Gas- and dual-radiator RICH

The large gas RICH on the hadron endcap is one most important systems of the EIC detector, but perhaps also the one offering most choices, the implications of which need to be fully understood before a final decision is made on which path to pursue. Since the challenges are very specific to the EIC, so is the required R&D. The most fundamental question is whether to build separate gas- and aerogel RICH detectors or use a dual-radiator RICH. However, within each of the two categories there is a natural set of choices.

The dual-radiator RICH is restricted to having mirrors that reflect the Cherenkov light outward (away from the beam). This is necessary, since the near-beam area on the hadron side has the highest radiation levels in the entire detector. This not only creates a lot of background hits, but the dose is too high for the currently available photosensors. This configuration also has the additional benefit that Cherenkov light produced in the gas does not have to pass through the aerogel. To enhance the signal, one could filter out the shortest wavelengths from the aerogel so that the collected UV light would only come from the gas. These photons undergo Rayleigh scattering as they pass through the aerogel, losing the Cherenkov angle information, and would only contribute to the noise if allowed to reach the focal plane. The simplest optics would consist of spherical mirrors arranged in sectors with 3D focusing, ensuring that the total photosensor area is small, as this is the main cost driver for this type of detector. While simple spherical mirrors do not produce a flat focal plane, which can introduce aberrations if not properly addressed, EIC R&D suggests that this is relatively straightforward to do by adjusting the layout of the photosensors. During the R&D phase, it thus does not seem necessary to If a sensor placement near the top of the hadron endcap would be preferable to a location close to the magnet coil, an additional mirror can be introduced moving the focal plane there. An advantage of the dual-radiator RICH is that it is easy to ensure full coverage both in angle and momentum – the latter by matching the refractive indices of the gas and aerogel (n=1.02 and C_2F_6 seems to be a very promising combination).

A gas-only RICH can in principle be built to the same geometry as dual-radiator RICH, but then there is no compelling reason for not simply add a second radiator. Thus, the main reason for choosing a gas-only RICH is to have inward reflecting mirrors (i.e., towards the beam). This choice changes the overall shape of the RICH detector from a
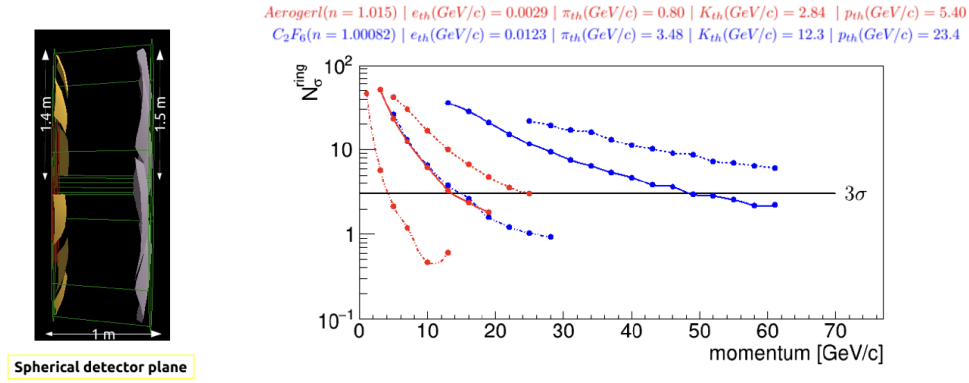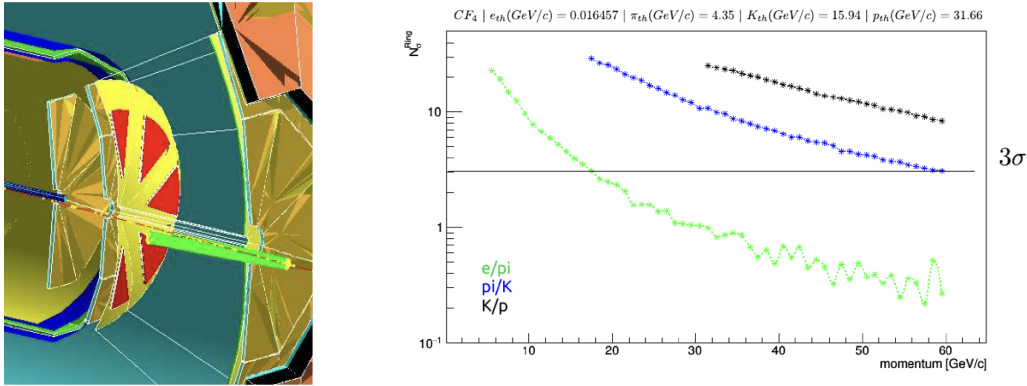
Figure 2.5: dRICH design and performance.

Figure 2.6: gasRICH design and performance.

cylinder ("pillbox") to a cone (without its top, and with a rounded bottom). Depending on the overall layout of the detector, this may be easier to integrate with the other subsystems. The radiation issue associated with inward-reflecting mirrors and a focal plane close to the beam is addressed by using GEM photosensors, which are more radiation hard than optical photosensors such as MCP-PMTs or SiPMs. The GEM photocathode is sensitive in the UV, which makes them a reasonable match for CF_4, which is the lightest of the gases typically used for Cherenkov detectors, which in principle should provide coverage up to the highest momenta. However, since the refractive index of the gas changes at short wavelengths, and we cannot measure the color of the photon, chromatic effects become the main source of uncertainty. These can be reduced by filtering out the shortest wavelengths, but at the price of a lower photon yield, which also contributes to the resolution.

An initial comparison carried out between the gas-only and dual-radiator RICH options indicated a comparable momentum reach using CF_4 gas in the former and C_2F_6 in the latter – both fulfilling the EIC requirements. The main difference is on the other side of the momentum range. When combined with an aerogel RICH, the lighter gas provides an overlap in coverage only in threshold mode for K/π and not at all for K/p. If continuous coverage would be desired, it may be possible to find an alternative gas or gas mixture, with a higher index of refraction, but retaining properties like transparency in the UV. It is

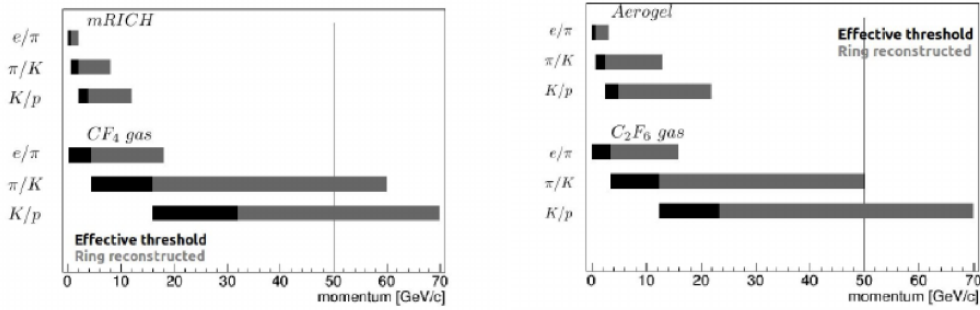also possible that in the future a photocathode sensitive to visible light could be developed.

Figure 2.7: gas- and dRICH comparison.

2.4.3 Modular Aerogel RICH

Proximity focusing aerogel RICH detectors provide reasonable performance in a reason-
ably small footprint. This can be improved by using two layers of aerogel with precisely
matched indices to create a focusing effect. However, while such a detector could be used
for the EIC, recent R&D suggest that cost, size, and momentum coverage could all be
improved by using lens focusing (a Fresnel lens would be preferable, but a spherical lens
could be an alternative). The latter naturally leads to a modular design (hence mRICH),
where each module has its own lens and readout. The main advantages of using a lens is
that it creates a smaller, but sharper ring image, and that it centers the ring in the middle
of the photosensor plane even if the hit was in a corner. This means that the photosensors
require a smaller pixel size ($2 - 3$ mm), but the area can be reduced, leading to improved
performance and reduced cost. In addition, a lens allows for more effective focusing,
which makes it possible to shorten the module. It also avoids complications of having
to very precisely match the refractive index of pairs of aerogel tiles to create the desired
focal length. The modular design makes the aerogel mRICH very flexible and easy to
integrate with the EIC detector. It also allows for a projective arrangement, which can
reduce the angular range of particle tracks impinging on the detector. This in turn further
reduces the required sensor area. One thing to keep in mind is that while the EIC R&D
currently focuses on one representative configuration to demonstrate the performance
of the mRICH, it would be quite easy to use different variations in different parts of the
EIC detector. For instance, while the prototype aims for 3σ K/π separation up to $8 - 9$
GeV/c, increasing the focal length and reducing pixel size will make a module slightly
longer but improve the performance. Longer modules can be used where there is space or
performance is essential, while shorter modules can be used where integration with other
systems imposes constraints on the overall geometry. In a similar way, different modules
can use different photosensors. For instance, modules placed closer to the beam could
use MCP-PMTs (which are more radiation hard), while modules further away could use
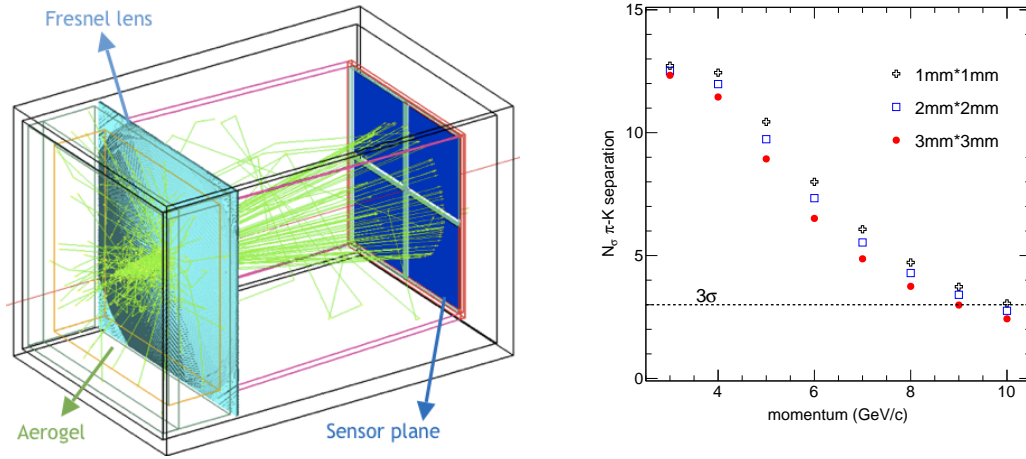SiPMs (which are not significantly affected by magnetic fields, regardless of angle).

Figure 2.8: mRICH design and performance.

2.5 Far forward detectors

Roman Pots will be necessary to measure the intact proton for exclusive diffractive observables such as deeply virtual Compton scattering and deeply virtual meson production. Far forward detectors will be needed since the intact protons are expected to scatter at small angles ($\leq$ 14 mrad). Measuring the scattering angle of these protons will be necessary for measuring variables such as Mandelstam t, which is equivalent to the square of the momentum transfered during the DIS process. Given the latest interaction region configuration as described in the eRHIC pre-CDR [cite], it will be possible to install Roman pots at +35~40[need confirmation for this number] meters from the nominal collision point. Two Roman Pots stations will be installed in this region, with each station being comprised of a vertical and horizontal substation in order to have full azimuthal coverage about the beam line. Each substation is further composed of two stacks of Si detectors located on opposite sides of the beam. The stacks are made of four 0.4 mm thickness Si micro-strip panels with an active area of 79 mm by 48 mm. Each plane should be oriented perpendicular to the adjacent plane(s) in order to measure the proton position along the x and y axes respectively. Our resolution on measuring t will largely be dependent on the spatial resolution of the Roman Pots detectors. This setup is identical to the instillation of Roman Pots detectors for the STAR experiment [cite] with the key differences being the location and number of Roman Pots detectors. [How close to beam they could be based on eRHIC pre-CDR?]

In order to tag spectator neutrons in collisions with light (or heavy) ions, a zero-degree hadronic calorimeter will be placed [describe location, also size/angular acceptance?].

2.6 Data acquisition

Jin Huang Modern electronics and computing development enable the experimental nuclear physics field to transition from the traditional triggered event-wised Data Acquisition (DAQ) to a DAQ model where time-stamped data is streamed from detector with event

forming in the online or offline computing [9]. Removing the layer of a hardware-based trigger in the data acquisition offers multiple advantages to an EIC experiment:

- Hardware trigger is effectively a cut on EIC events in the hardware layer. This leads to added systematic uncertainty that stems from the reproducibility of the hardware trigger in analysis and the loss of information for events that failed the hardware trigger condition.

- A free streaming DAQ model allows access all EIC events in a minimal-biased manor, which translates to improvement over both statistical and systematical uncertainties.

- It is challenging to design hardware trigger due to the versatility of EIC collisions, which includes large fractions of diffractive and exclusive cross sections and physics. Meanwhile, the streaming readout DAQ allows software-trigger based upon the full and calibrated detector information as the one accessed by analysis.

- Certain detector subsystem technologies take long response time when compared with the EIC event spacing, which leads to duplicated data or dead time in an event-building DAQ. In particular, the Time Projection Chamber requires 10-30 us to readout one full event [10], which is much longer than the average EIC collision spacing at 500kHz collision for a top instantaneous luminosity of 10^34 cm^{-1}s^{-1}. Recording EIC events higher than 100 kHz would incur significant duplication of TPC hit-time segments. For such detector, it is much economical to record data in a streaming manor.

The main challenge for the streaming type of DAQ is to implement it in an affordable and reliable way. Therefore, the subsystem multiplicity distribution (Figure 2.9, 2.10, and 2.11) and the average data rate (Figure 2.12) are studied in a simulation study combining the eRHIC tune of PYTHIA6, which represents 50 μb of the $e+p$ collisions, and the full detector GEANT4 simulation of sPHENIX-based EIC detector. At the top instantaneous luminosity of 10^34 cm^{-1}s^{-1}, the trigger-less zero-suppressed streaming data rate from the EIC collision is around 100 Gbps, which is the minimal amount of raw data that to be recorded to disk for recording all minimal bias EIC collision without the assumption of online reconstruction. This total signal data rate fit well within the designed DAQ disk-writing bandwidth for the sPHENIX DAQ, which is at least 200 Gbps [10].

We do note this data rate estimation does not include background, e.g. beam gas collisions and detector noise, which could be significant depending on the accelerator and detector design and the running conditions. This important missing factor require further study to quantify, such as those being addressed at eRD21 [11] and by the eRHIC design team [4]. Meanwhile, FPGA- and CPU-based real-time computing power built into the DAQ may be able to filter out significant of such background hit within the DAQ system.

The EIC detector based on the sPHENIX experiment would benefit significantly by inheriting and augment upon the sPHENIX DAQ:

- The tracking detectors of sPHENIX, i.e. MAPS-based vertex detector, Time Projection Chamber, and the silicon strip tracker, intrinsically support trigger-less streaming readout in their front end electronics [10].

- The sPHENIX DAQ throughput rate of 200 Gbps would easily accommodate the streaming data from the EIC collisions at 10^34 cm^{-1}s^{-1} as discussed above. This also allow the experiment to record all zero-suppressed raw data from detector without the requirement of online data reconstruction. Nevertheless, partial online
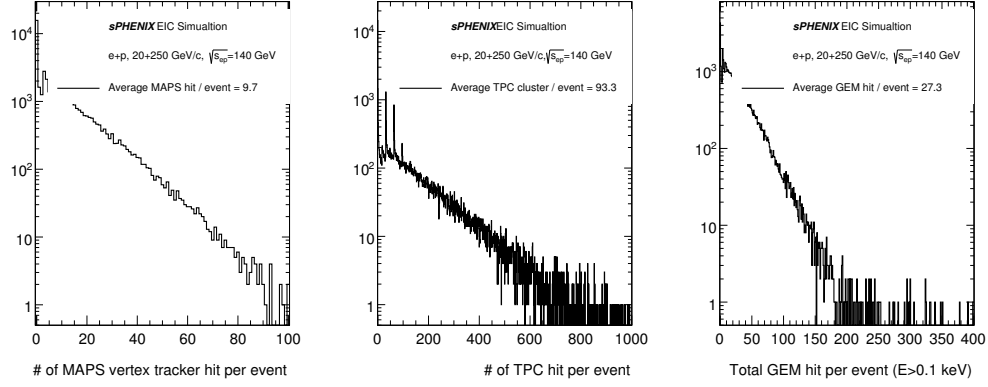
Figure 2.9: Distribution of number of hits in the tracking detectors that originated from single $e+p$ collision at $\sqrt{s_{ep}} = 140$ GeV.
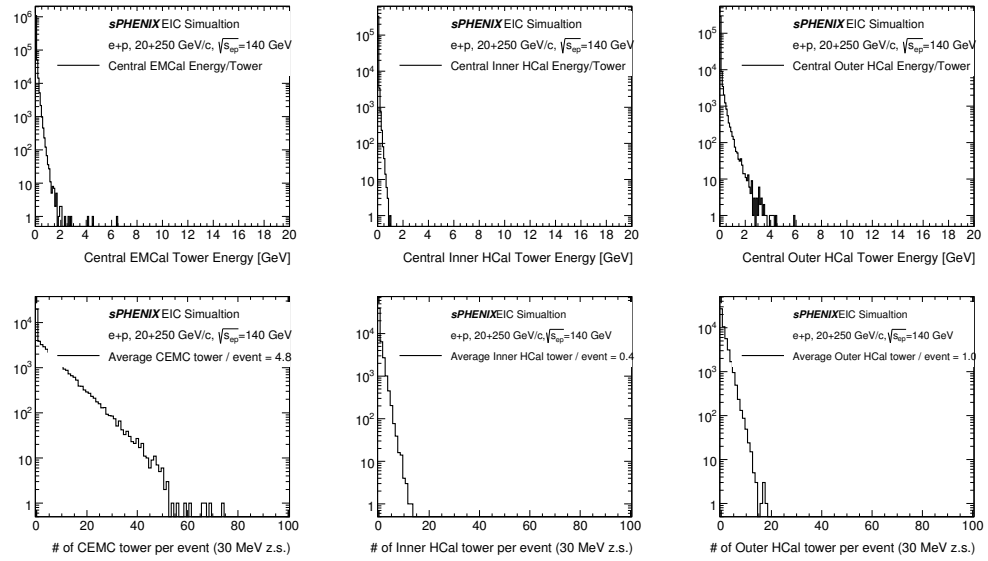

Figure 2.10: Distribution of per-tower energy and the number of active towers in the central calorimeters that originated from single $e+p$ collision at $\sqrt{s_{ep}} = 140$ GeV.
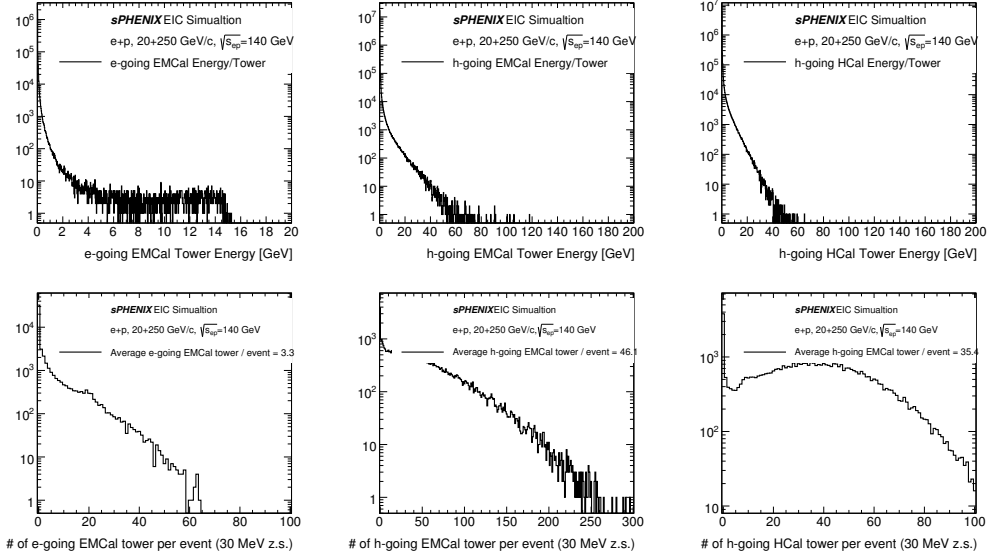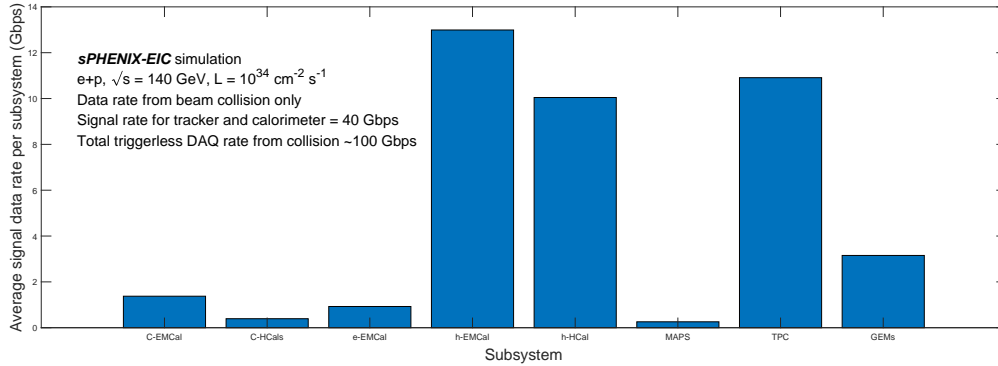
Figure 2.11: Distribution of per-tower energy and the number of active towers in the forward calorimeters that originated from single $e+p$ collision at $\sqrt{s_{ep}} = 140$ GeV.

Figure 2.12: Trigger-less DAQ data rate breakdown to subsystems that originated from $e+p$ collisions at $\sqrt{s_{ep}} = 140$ GeV and instantaneous luminosity of $10^{3}4$ cm^{-1}s^{-1}. The primary collision events are generated via eRHIC tune of PYTHIA6, which represents 50 μb of the $e+p$ collisions. All generated particles are then simulated via full detector GEANT4 simulation which is ten converted to streaming data rate. Only tracker and calorimeters are included in this simulation study which sum to a collision-originated streaming data rate of 40 Gbps. With addition of the PID detectors, the overall collision-originated streaming data rate would be around 100 Gbps. Please note the background, e.g. beam gas collisions and detector noise, are not included in this study, which could be significant depending on the accelerator design.

1   data reconstruction would be beneficial to the experiment to QA the data and to
2   speed up the analysis cycles.
3   • The majority bandwidth in the sPHENIX DAQ is routed through the a high-
4   throughput FPGA-based PCIe card, Front-End LInk eXchange (FELIX) card, which
5   bridge the detector specific electronics and the commodity computing [12]. Such
6   architecture is also planned for the ATLAS, LHCb and ALICE Phase-I upgrade
7   and beyond [12, 13, 14]. Therefore, the FELIX-based sPHENIX DAQ architecture
8   would be used by the large collider experiments at the time of EIC, year 2025 and
9   beyond.
10   • The major additional work is updating the FPGA firmware and DAQ software to
11   record time-segmented data streaming, instead of the final event-building steps of
12   the current sPHENIX DAQ.
13 Therefore, in this letter we propose to reuse the FELIX-based sPHENIX DAQ with only
14 modification in firmware and DAQ software, and without the need of significant new
15 hardware investment.

3. Detector Performance

This chapter summarizes the performance evaluation of the EIC detector based on sPHENIX described in Chapter 2. The studies use a full GEANT4 simulation of the experiment (see Fig. 3.1) and detector performance parametrization based on GEANT4 simulation studies. Section 3.1 addresses the charged particle tracking resolution. Section 3.2 quantifies the expected energy and angular resolution for measuring jets with this EIC detector based on sPHENIX. Section 3.3 describes DIS kinematics reconstruction. Section 3.4 illustrates particle identification performance. Section 3.5 discusses charm tagging capabilities. Section 3.6 studies the performance of the detector to reconstruct DVCS events. Finally, Sec. 3.7 studies the reconstruction of J/ψ mesons from their decay into electron-positron pairs.
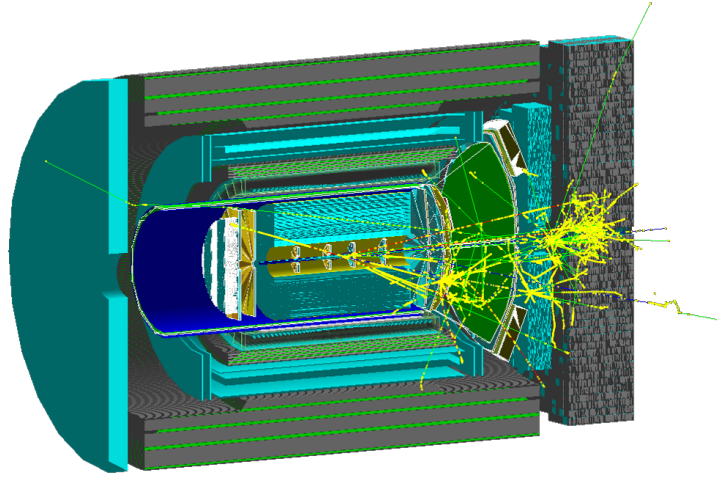
Figure 3.1: A simulated DIS event in the GEANT4 detector description with $Q^2 \sim$ 100 GeV^2 in an $e + p$ collision with 18×275 GeV. The sPHENIX experiment with proposed forward instrumentation in GEANT4. The central tracker is approximated as a generic four-layer silicon-based tracking system with two small vertex GEM tracking stations in the forward direction.
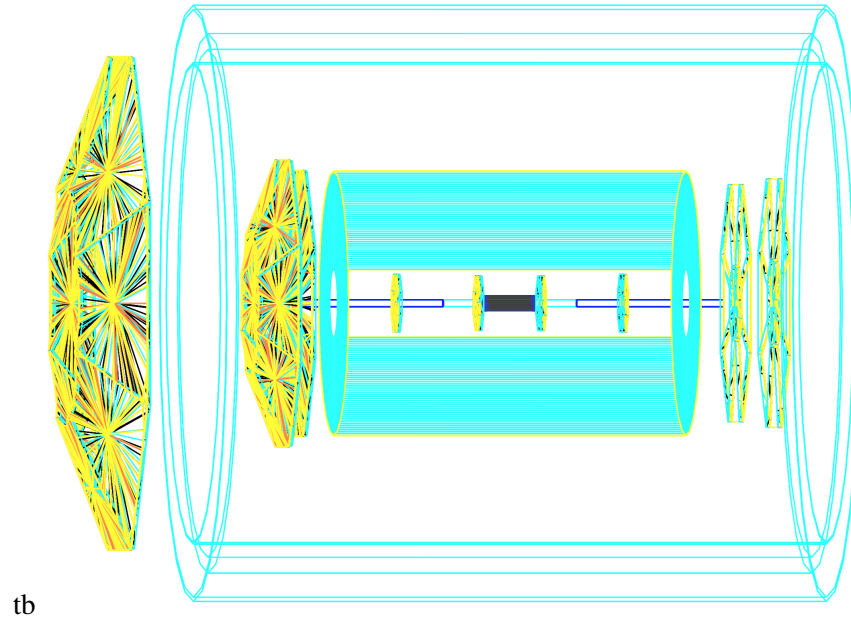
tb

Figure 3.2: Geant4 model of tracking detectors setup. Detectors are drawn in scale. Yellow wireframes depict the forward/backward GEMs stations. Light-blue volume represents the Time Projection Chamber. Black cilinder close to interaction point shows the extension of the MVTX detector. In this drawing positive z is to the left side.

3.1 Tracking Performance

The tracking detector's geometry was implemented into sPHENIX geant4 simulation framework. Figure 3.2 is a drawing from the geant4 visualization toolkit showing the tracking detectors used. The tracking detectors have been fully explained in chapter 2; nevertheless, in the following paragraphs, a brief description of each detector realization in the simulation is provided.

The Silicon Vertexer (MVTX)

The geometry used considers the most up-to-date description with 3 layers of silicon detectors extended using ALICE's upgraded ITS stave stations configuration (REF) using a realistic material budged. For the present simulation, the sensitive pads are considered fully efficient and a constant position smearing in rφ-z plane ($5x5$ μm^2) on the hit is used to account for clusterization.

The Time Projection Chamber (TPC)

A Ne-based gas is used inside the chamber volume which extends from 20cm to 80cm in radius. Both inner and outer field cages were included in the material budget. The hits in the sensitive volume where smeared in the rφ direction (150 μm) in order to account for the pad segmentation and in the Z direction (0.5 mm) in order to mimic the time resolution from the electronics readout.
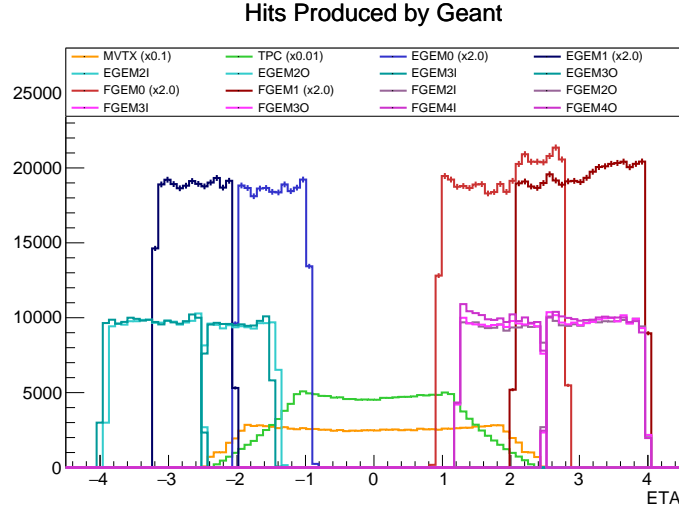
Figure 3.3: Breakdown of pseudorapidity distribution of hits per detector.

Forward (FGEMs) and backwards (EGEMs) Tracking Detectors

A Methane-GEM based tracking stations are used for both forward (hadron going side - FGEM) and backwards (electron going side - EGEM). The material budget for the enclosing was also included in each station. The EGEM set consist of 4 stations named EGEM0, EGEM1, EGEM2 and EGEM3, while the FGEM set has 5 stations (FGEM0, FGEM1, FGEM2, FGEM3 and FGEM4). In the last two (three) stations of the EGEM (FGEM) set, there is a subdivision into inner and outer sections depending on pseudorapidity where the pad segmentation changes so that the position resolution improves at the highest pseudorapidity: -2.5 for EGEM and +2.5 for FGEM.

$- \cdot -$

Figure 3.3 shows the pseudorapidity distribution of hits produced in the sensitive volume of the detectors. EGEM2-3, FGEM2-4 have been divided into two section at $\eta = -2.5$ and $\eta = +2.5$, respectively. Notice that EGEM0 and FGEM0 overlap by about 0.2 units of pseudorapidity with the fully efficient coverage of the TPC and aids as the tracks leave the edges of the central trackers. Table 3.1 summarizes the parameters used for resolution in each tracking detector. Figures **??** show a hit map of the various detectors and the distribution of smearing used for clusterization of the hits.

Once the clusters have been identified they are fitted using the Kalman Filter procedure from the GenFit package (REF). This process takes the clusters and covariances from each detector plane and performs a iterative fit of the clusters using as reference the trayectory of a track propagating through the detector considering its energy loss in material and bend due to the magnetic field.

Figure 3.1 demonstrates the momentum resolution of the system when firing μ-ons at different pseudorapidity values. As can be seen, the momentum resolution decreases at higher momenta which is due to our ability to measure the sagita for a *mu*-ons bending with a big radius of curvature in such constrained space. On the other hand, for small momentum, the resolution is limited by multiple scattering and so we obtain out best resolution for particles close to midrapidity where our detector setup has the less material

	σ_R (mm)	$\sigma_{R\varphi}$ (μm)	σ_Z (μm)	Efficiency (%)	Noise (%)
MVTX	–	5	5	100	0
TPC	–	150	500	100	0
EGEM0	10	50	–	100	0
EGEM1	10	50	–	100	0
EGEM2 Inner	10	50	–	100	0
EGEM2 Outer	10	100	–	100	0
EGEM3 Inner	10	50	–	100	0
EGEM3 Outer	10	100	–	100	0
FGEM0	10	50	–	100	0
FGEM1	10	50	–	100	0
FGEM2 Inner	10	50	–	100	0
FGEM2 Outer	10	100	–	100	0
FGEM3 Inner	10	50	–	100	0
FGEM3 Outer	10	100	–	100	0
FGEM4 Inner	10	50	–	100	0
FGEM4 Outer	10	100	–	100	0

Table 3.1: Tracking detector properties
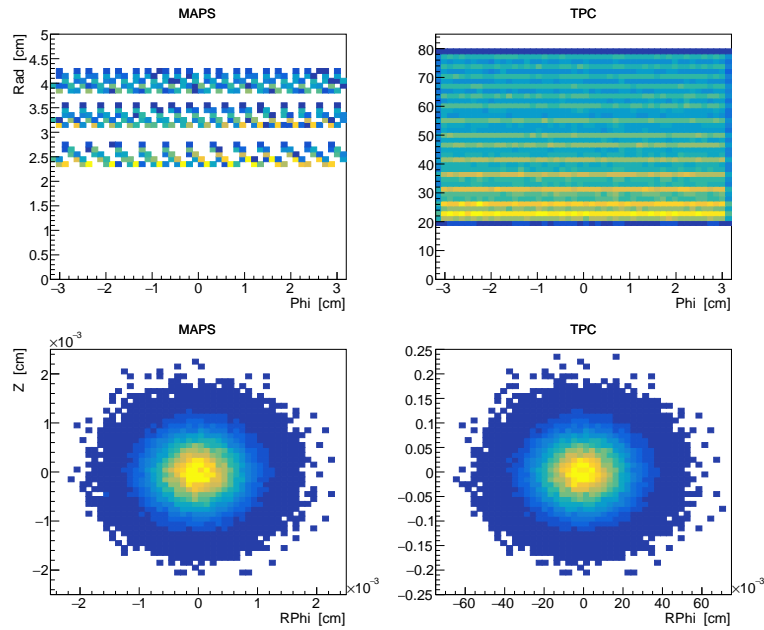
Figure 3.4: Central Tracker. TOP: Hit density distribution in phi and rad coordinates. BOTTOM: Distribution of deviations from true hit position.
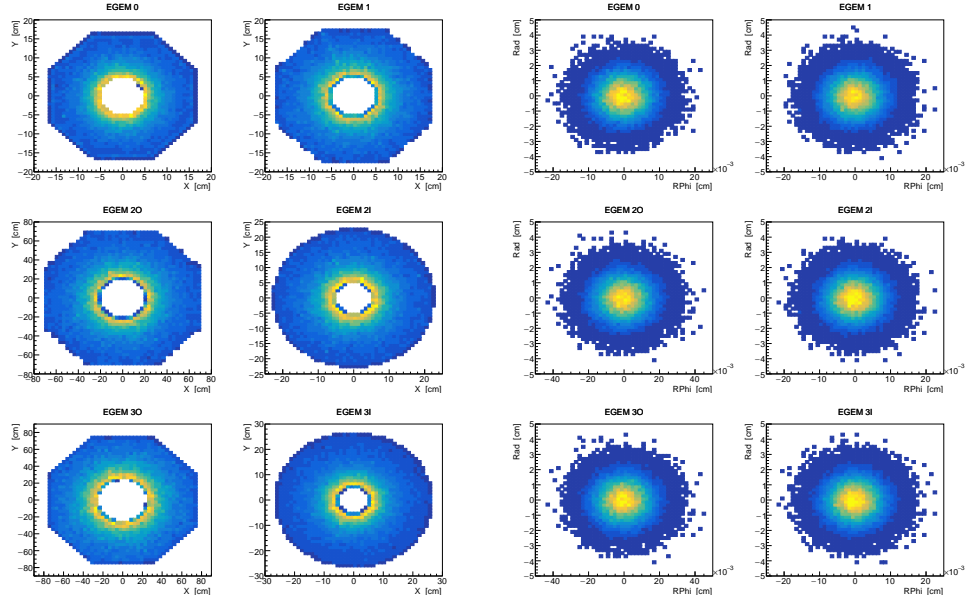
Figure 3.5: Negative eta (electron going) tracker. LEFT: Hit density distribution in phi and rad coordinates. RIGHT: Distribution of deviations from true hit position.
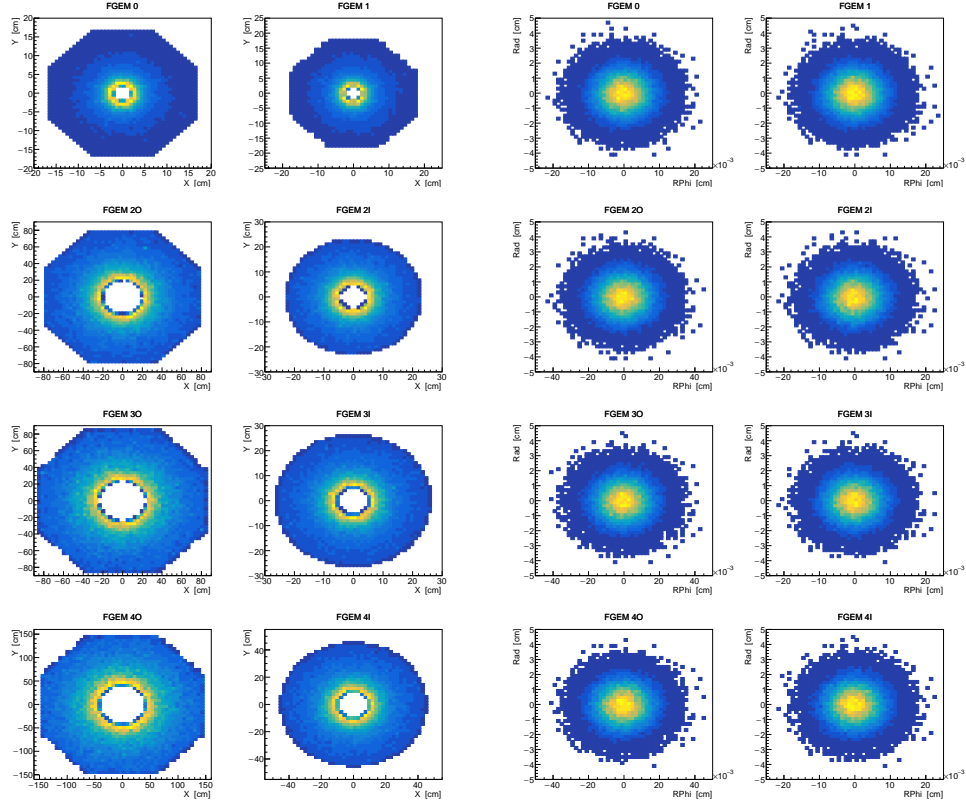

Figure 3.6: Positive eta (Hadron going) tracker. LEFT: Hit density distribution in phi and rad coordinates. RIGHT: Distribution of deviations from true hit position.

budget possible (TPC gas) going down below to 1% at 1 GeV/c.

It is worth noticing that even though the FGEM and EGEM stations have different spatial extent at low momentum the resolution seems mainly driven by the material budget and not by the different lever arm in the system. However at high momentum, there is a big improvement in the FGEM setup due to its bigger extension. In either case, for high momentum as the trajectory of the particle approaches the beamline (large η), the momentum resolution drops off sharply.

All of these features can be folded into a simple parametrization of the momentum resolution. Figure 3.1 shows a fit to the momentum dependence of the resolution for different pseudorapidity bites. For the fit a combined description of multiple scattering a (constant uncertainty) and lever arm b (linear uncertainty) was employed:

$$\frac{\sigma_p}{p} = a \oplus b \cdot p \tag{3.1}$$

The variations of the two parameters a and b in Eq. 3.1 for each fit is shown in figure 3.1. Notice that the Multiple Scattering term (param1) is very symmetric with respect to 0, which can be associated at the similar material budged on both sides for the GEM stations. The Lever Arm term (param2), however, shows a slighted distorted symmetry which accounts for the fact that the FGEM has a bigger extension and thus help improve on the sagita estimation. Notice also that around $|\eta| = 1$ there is an improvement in the momentum resolution obtained with the aid of the first vertical GEM stations on both sides.
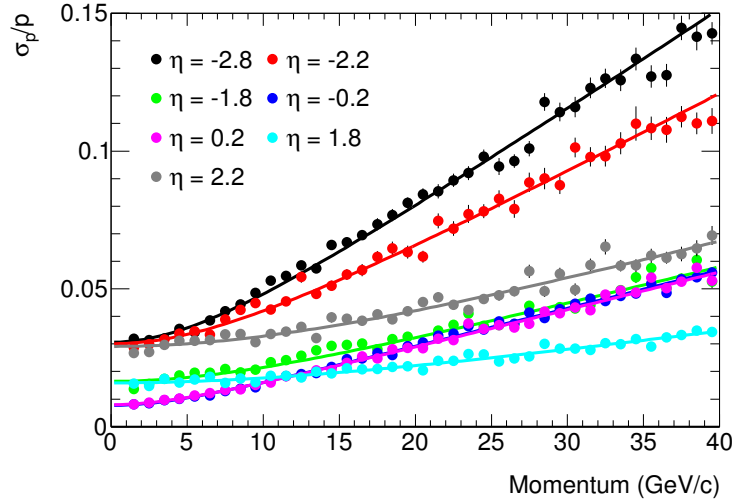

Figure 3.7: Momentum resolution from GEANT4 as function of momentum for different pseudorapidities. Fit function is Eq. 3.1.
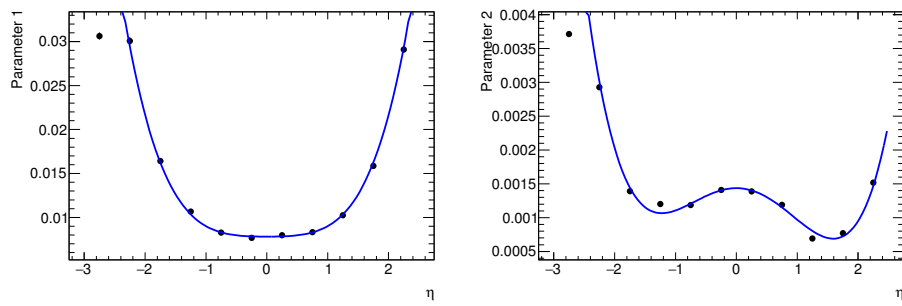
Figure 3.8: Fitting parameters *a* (left) and *b* (right) from fits in Fig. 3.1 with polynomial fits.

3.2 **Jet Reconstruction**

Jet has been proven to be a powerful tool in particle physics, especially in high-energy collider experiments. Comparing to final state hadrons, jet is usually a better approximation of the scattering partons. With the Electron-Ion collider, jets production will definitely be of importance for different physics measurements. In this section, we have been focused on the capability of jet reconstruction within the current detector design.

By using the PYTHIAeRHIC generator, the electron–proton MC events were generated for three collision energies, 10×100 GeV^2, 10×275 GeV^2, and 18×275 GeV^2, where the Q^2 was limited between 10 and 10^4 GeV^2. The generated MC events were subsequently passed through the full detector simulation module based GEANT4. Jets were reconstructed from the calorimeter system responses, including the Electromagnetic and Hadronic Calorimeters in both Barrel region and hadron going forward region, by using the FASTJET package. The jet reconstruction capability was studied by comparing the matched jets from generator level which is denoted as "true" jet and detector level which is denoted as "reco" jet.
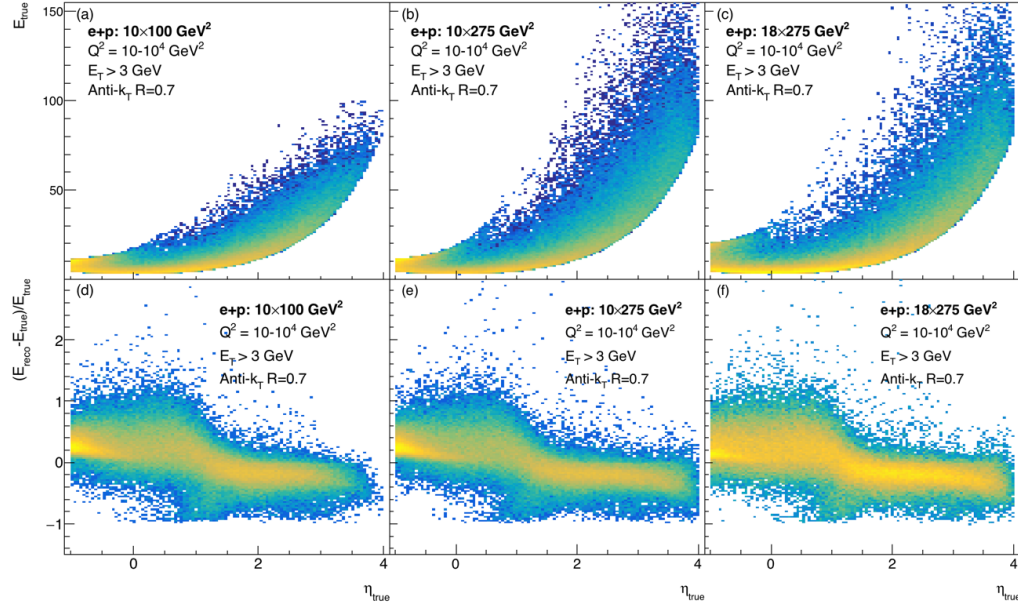

Figure 3.9: True jet energy and the energy ratio of "reco" jets over "true" jets vs. pseudorapidity for different collision energy: (a)(d) e+p = 10×100 GeV^2, (b)(e) e+p = 10×275 GeV^2, (c)(f) e+p = 18×275 GeV^2.

Figure 3.9 (a)-(c) show the "true" jet energy distributions as function of jet pseudorapidity for different collision energies. The transverse energy E_T has been required to be greater than 3 GeV. It can be found that the high energy jets are predominantly produced at the proton-going direction and the scattered electron is significantly contributing to the jet reconstruction at electron-going direction. Figure 3.9 (d)-(f) are the corresponding energy ratio of "true" jets over "reco" jets, where we can see the clear difference between barrel region ($-1 < \eta < 1$) and forward region ($1 < \eta < 4$).

For forward region, the number of particles per jet as a function of the transverse
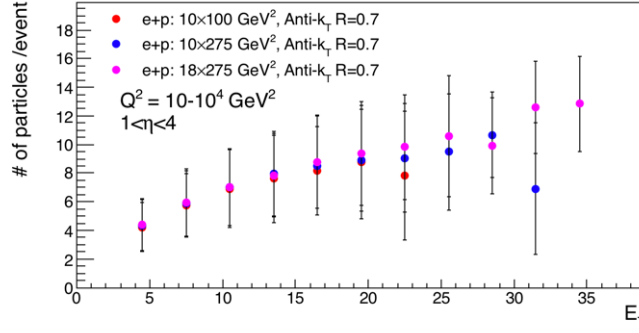
Figure 3.10: Number of particles per jet with particle $E_T > 0.2$ GeV for different collision energies at forward pseudorapidity, $1 < \eta < 4$.

energy are shown in Figure 3.10 for different collision energy. The number of particles in one jet shows strong dependence on jet transverse energy but no dependence on the collision energy.

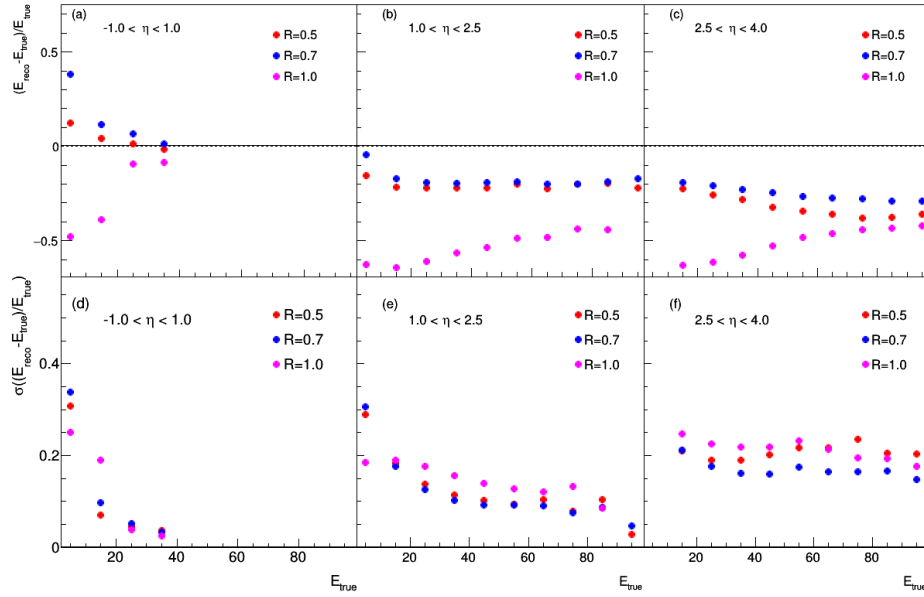Figure 3.11: Energy scale shift, mean value of $(E_{reco} - E_{true})/E_{true}$, as a function of E_{true}; and energy resolution, width of $(E_{reco} - E_{true})/E_{true}$ distribution from Gaussian fit, as a function of E_{true} for different η ranges: (a)(d) for $-1 < \eta < 1$, (b)(e) for $1 < \eta < 2.5$, and (c)(f) for $2.5 < \eta < 4$.

Figure 3.11(a) shows the middle rapidity jet energy scale shift, the mean value of $(E_{reco} - E_{true})/E_{true}$, as function of E_{true} for jet cone radius $R = 0.5$, 0.7, and 1.0. At lower energy region, the energy scale is more sensitive to the jet cone size likely due to the contribution from detector noises. Around $E_{true} = 20$ GeV, the energy of the beam electrons, the reconstructed jet energy are quite close to the true jet energy and

1 stable as cone size changing. From Fig 3.9(c), it can be found that the 20 GeV jets peak
2 around $\eta \sim -1$. Figure 3.11(d) shows energy resolution, width of $(E_{reco} - E_{true})/E_{true}$
3 distribution from Gaussian fit. For forward region, Fig 3.11(b), (c), (e), and (f) show the
4 energy scale shift and resolution as function of E_{true}. I can be found at more forward
5 region the energy resolution gets worse. The η and ϕ resolutions are shown in Fig. 3.12,
6 (a)-(c) and (d)-(f) respectively. The η and ϕ resolutions are improved as the energy
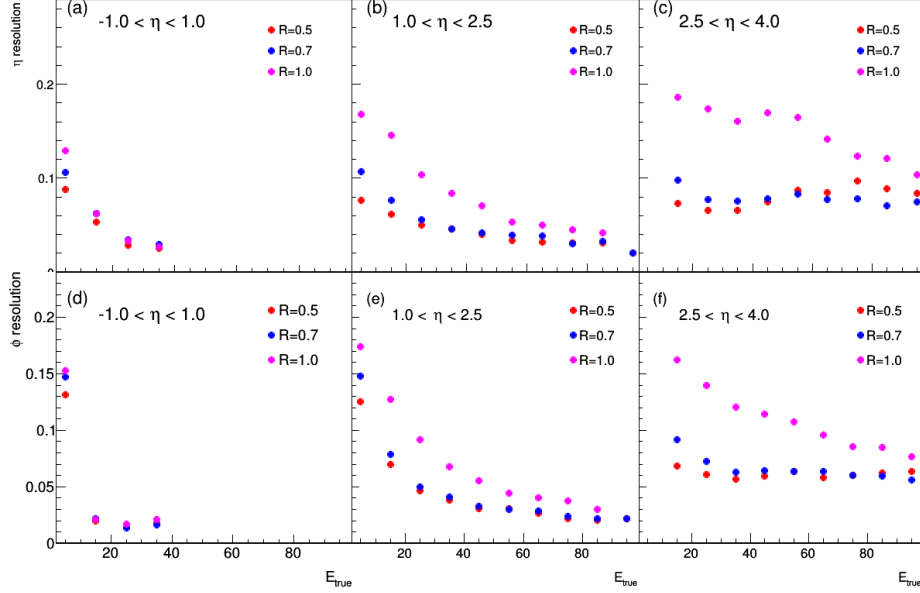7 increasing.

Figure 3.12: Jet η reconstruction (a) and ϕ reconstruction(b) with jet cone radius $R = 0.7$ at $\sqrt{s} = 140$ GeV.

8   In summary, we learned from this study that jet can be effectively reconstructed with
9 reasonable energy resolution by only using the calorimeter system in the η range from -1
10 to 4. At low energy region, the jet reconstruction is expected to be significantly improved
11 after including the tracking system, e.g. TPC and GEM. Further including particle flow
12 information, we will be able to study the jet mass reconstruction as well as the physics
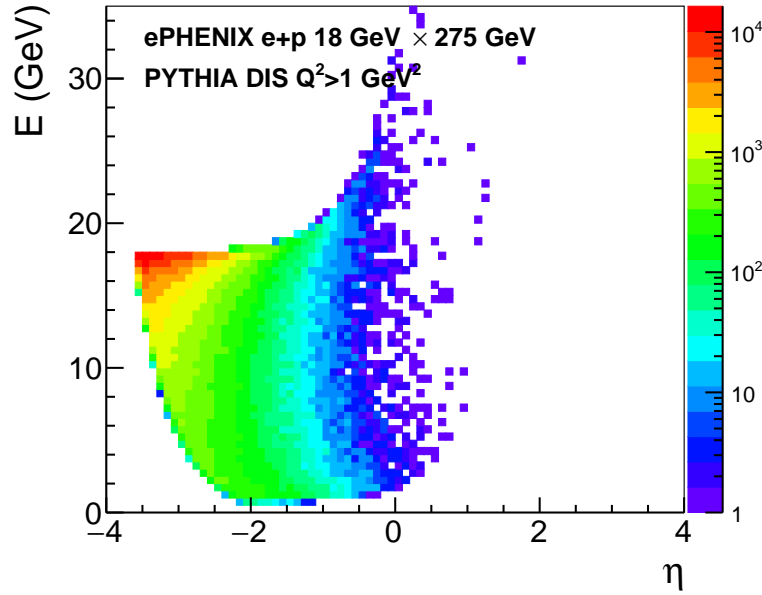13 impact estimates for different physics processes.

Figure 3.13: Distribution of scattered electrons in pseudorapidity and energy. The results are from PYTHIA DIS simulations for $e+p$ collisions with 18 GeV $\times$ 275 GeV beam energies. The events are selected as DIS with $Q^2 > 1$ GeV^2.

3.3 DIS Kinematics Reconstruction

DIS kinematics reconstruction in NC reactions (through virtual photon and Z-boson exchange) can be done via measurements of the scattered electron ("electron" method). Reconstruction of the hadronic final state is an alternative approach ("hadronic" or Jacquet-Blondel method) which provides different resolutions compared to "electron" method, in some (x, Q^2) regions better and in the other regions worse than the "electron" method. Different hybrid approaches combining measurements of scattered electrons and produced hadrons usually provide the optimal way to reconstruct DIS kinematic variables. In CC DIS (through $W^{\pm}$ boson exchange) hadronic method is the only possible one, as in such reactions a scattering electron turns into an unmeasured neutrino.

3.3.1 Electron identification

"Electron" method requires high purity identification of scattered electrons. Fig. 3.13 shows that electrons are scattered mainly in the direction of the electron beam. The scattered electron energy varies from zero to approximately the electron beam energy. Scatterings in the barrel region correspond to higher Q^2 reactions, where the scattered electron energy can exceed the electron beam energy gaining momentum from the collision with the higher momentum hadron beam.

Collider kinematics allow separation of the scattered electrons from other DIS fragments – hadrons and their decay products – which are detected preferably in the h-going direction, leaving much softer spectra in the central region and the e-going direction.
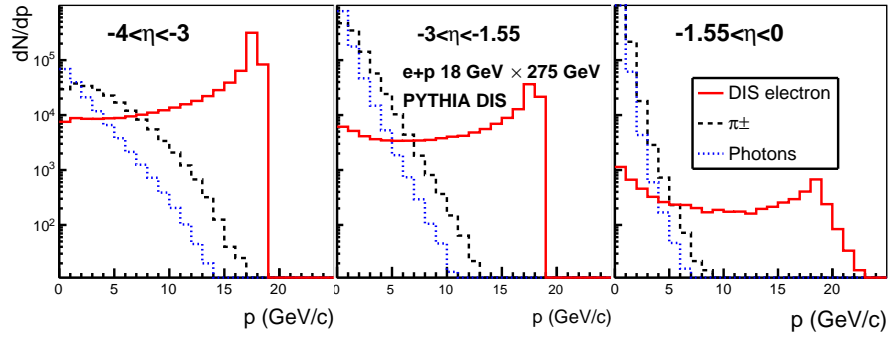
Figure 3.14: For 18 GeV $\times$ 275 GeV beam energy configuration: Momentum spectra for scattered electron (red), charged pions (black) and photons (blue).

Fig. 3.14 shows scattered electron momentum spectra along with photon (mainly from hadron decays) and charged pion spectra. Hadronic and photonic backgrounds are small at higher momenta, but increase rapidly at lower momenta.

EMCal alone provides a powerful mean for electron ID and hadronic background suppression, as a charged hadron deposits in the EMCal either low energy as a MIP particles or a fraction of its energy in case it initiates hadronic shower in the EMCal. Charge particle track reconstruction helps to identify photon background and provides additional tool for charged hadron background suppression through the E/p matching, when comparing track momentum from the tracking system with the energy of the associated cluster in the EMCal.

Fig. 3.15 shows the effectiveness of the charged hadron background suppression. Evaluation was done using parameterized tracking system momentum resolution (see Sec.*) and full GEANT simulation of electron and hadron response in the EMCal, which for the barrel EMCal was confirmed through the test beam data. High purity electron identification is provided for electron momenta >3 GeV/c (>2 GeV/c) for 18 GeV (10 GeV) electron beam, which only marginally limits the (x, Q^2) space probed with our detector, see Fig. 3.16. Transverse shower profile evaluation and information from HCal (in barrel region) are expected to further enhance the electron ID, which are not yet included in this study.

Electron-positron pairs from photon conversion in material between the collision point and the tracker will be another source of the background, which will be well identified by our tracking system in the magnetic field and additionally suppressed by E/p matching cut. A detailed GEANT simulation study is ongoing to quantify this effect.

3.3.2 x and Q^2 resolutions

Measuring scattered electron in NC DIS allows us to reconstruct the basic DIS kinematic variables x, y, and Q^2, fully characterizing the inclusive reaction. According to Eq.* it requires measurements of the scattered electron energy and polar angle θ_e relative to the electron beam direction. They are determined from the combination of the information from electromagnetic calorimeters and tracking system.

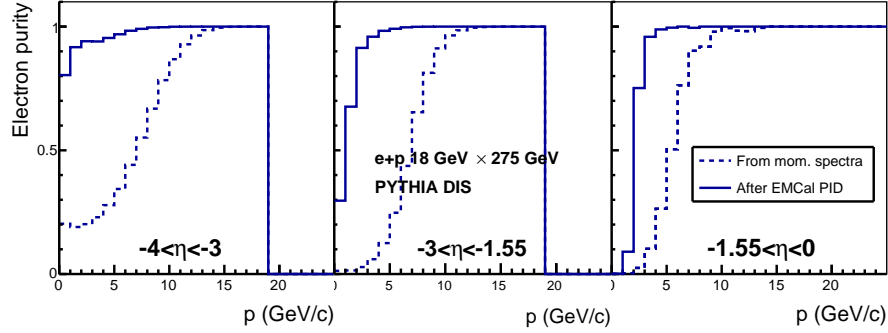In the barrel region, the high resolution tracking of sPHENIX detector will provide

Figure 3.15: For 18 GeV × 275 GeV beam energy configuration: The fraction of charged particles from DIS electrons before electron identification (dotted) and after identification with the EMCal+Tracking (solid).
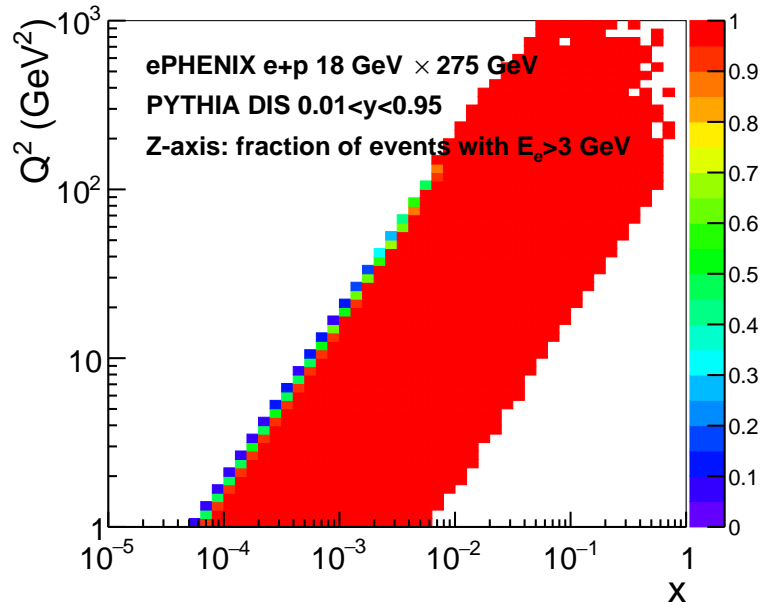

Figure 3.16: For 18 GeV × 275 GeV beam energy configuration: The color axis indicates the fraction of events in (x, Q^2) space surviving after a > 3 GeV energy cut on the DIS scattered electron.
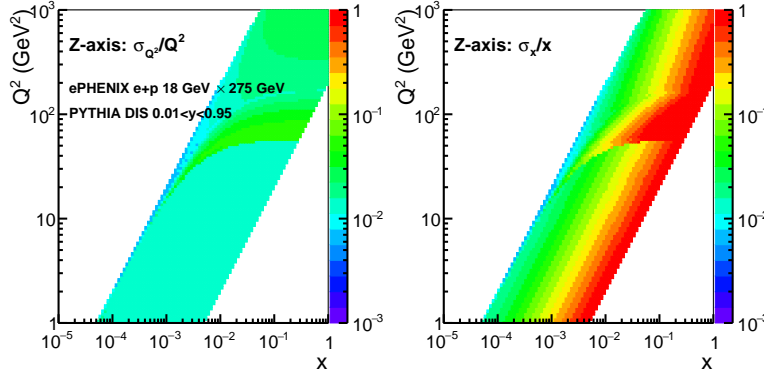
Figure 3.17: For 18 GeV $\times$ 275 GeV beam energy configuration: the relative resolution for Q^2 (left) and x (right) as a function of (x,Q^2).

high precision measurements of the scattered electrons, for both momentum and angle θ_e. In forward direction, due to reduced $\int (B_\perp)dl$ in the magnetic field of the barrel solenoid, and correspondingly larger multiple scattering effect in the momentum resolution of tracking system, the high resolution crystal EMCal will be a key detector for the measurements of the scattered electrons.

Fig. 3.17 shows the relative resolution for x and Q^2 as a function of (x,Q^2). Below we will show how it projects on the bin survivability distribution, and that the relative resolution of 10% is expected to satisfy the requirements. While the relative resolution σ_{Q^2}/Q^2 is defined mainly by the energy or momentum resolution σ_E/E, the resolution σ_x/x is proportional to $1/y$, which reflects as a diagonal-like dependence in (x,Q^2) space. The contribution of θ_e angle resolution is negligible for x and Q^2 measurements in both barrel and forward regions. The steps in resolution correspond to transition from barrel EMCal to high resolution crystal EMCal (at $\eta \sim -1.5$) and from high resolution barrel tracking to forward tracking (at $\eta \sim -1$).

Fig. 3.18 shows how these resolutions are translated to the statistical survival probability in a bin, which is calculated for 5 bins per decade in x and Q^2. This is calculated as a probability for an event to remain in its true (x,Q^2) bin. From the HERA experience, in such binning the survivability of >80% is expected to provide good precision for (x,Q^2) reconstruction, with capability to correct the smearing effect with high precision using the unfolding technique.

QED radiative effects (radiation of real or virtual photons) are another source of smearing. Unlike energy-momentum resolutions which introduces Gaussian-like smearing, radiative corrections are tail-like. They can be responsible for as much as 10-20% of statistics migrating away from a bin, and dominate over energy-momentum smearing at higher y.

The Jacquet-Blondel method, using the all final state particles except the scattered electron, is an alternative approach to reconstruct DIS kinematics. Kinematic reconstruction with the Jacquet-Blondel (JB) method is defined as:
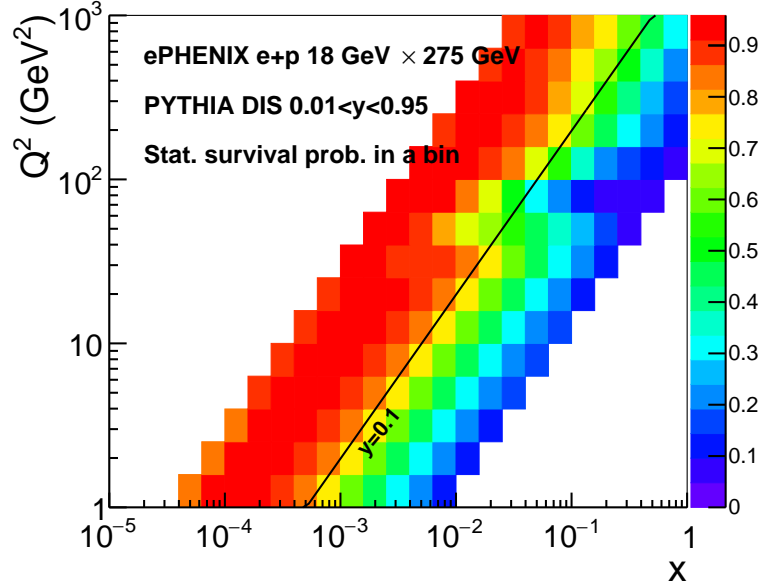
Figure 3.18: For 18 GeV × 275 GeV beam energy configuration: Statistics survivability in (x, Q^2) bins.

$$y_{JB} = \frac{\Sigma_i (E_i + p_{z,i})}{2E_e}, Q_{JB}^2 = \frac{p_{T,i}}{1 - y_{JB}}, x_{JB} = \frac{Q_{JB}^2}{s y_{JB}} \qquad (3.2)$$

where E_e is the incoming electron beam energy, and $p_{T,i} = |\Sigma_i \vec{p}_{T,i}|$, which is the total transverse momentum of the final state particles. [Ref*] At large momentum transfer DIS processes receive significant electroweak contribution. Neutral-current DIS is mediated either by a photon or a neutral weak boson, where there is a scattered electron that is used for kinematic reconstruction using the electron method. However, in charged-current DIS, mediated by a charged weak boson, the scattered lepton is a neutrino that is not detected. This leaves the event kinematics to be calculated only from the observed final state particles as defined in Eq.* using JB method.

To study the use of JB kinematic reconstruction both neutral-current and charged-current DIS events are generated using PYTHIA. One million events were generated with beam energies of 18 GeV x 275 GeV for the electron and proton respectively. Reconstruction of the kinematic variables from the observed final state particles in the detector acceptance depends on the resolution of the detector. Therefore, final state particle energies and momenta within detector acceptance were smeared according to parametrized resolutions from the results of GEANT4 simulations. Currently, tracking parametrization being used is from the BeAST detector and further studies with updated parametrization are ongoing.

For neutral-current DIS event kinematic reconstruction the JB method is particularly effective in the region of high Q^2 corresponding to the barrel acceptance, where the
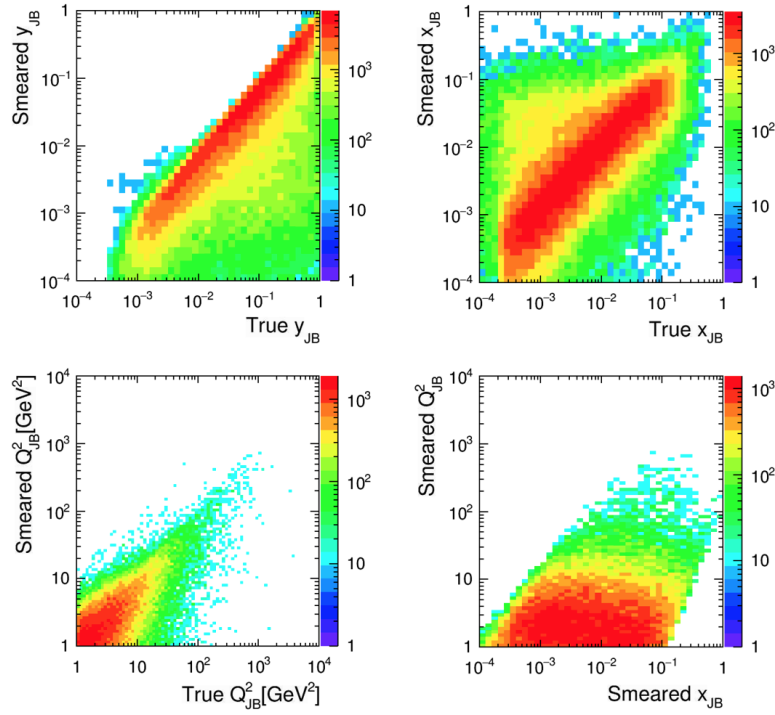
Figure 3.19: Top graphs and bottom left graph are correlations between the reconstructed kinematic variables y_{JB}, x_{JB}, and Q^2_{JB} and the smeared reconstructed kinematic variables. The lower right plot is the x, Q^2 smeared range of charged-current DIS. All events are generated in PYTHIA with electron and proton beam energies of 18 x 275 GeV including radiative effects with parametrized smearing.
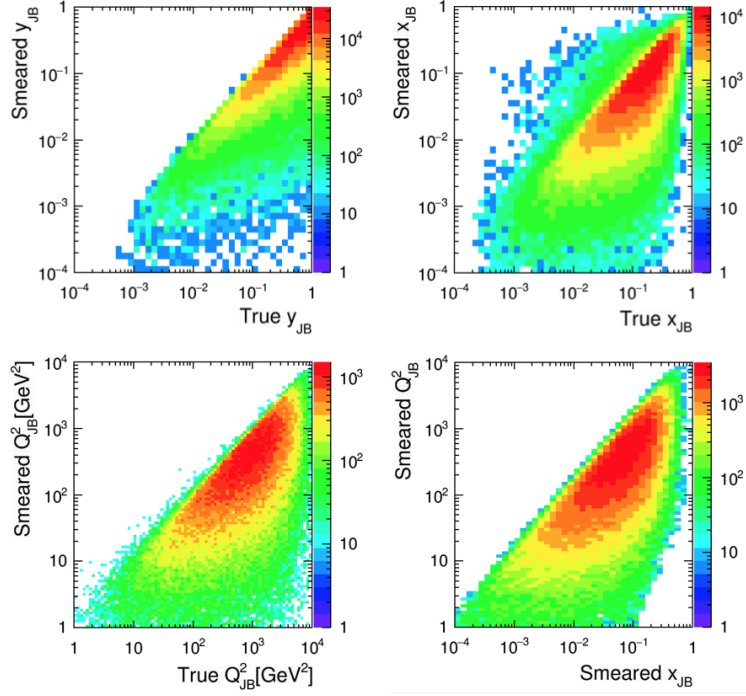
Figure 3.20: Caption. Note: CCDIS kinematic reconstruction and xQ2 range. With BeAST parametrization. Need to be updated.

resolution of the "electron" method is limited by the EMCal resolution. Moreover, unlike electron method with $\sigma_x/x \sim 1/y$, its resolution for x is nearly flat, so it provides better precision for x determination than the "electron" method in the region of small y.

[Insert figure for CC DIS kinematic reconstruction with JB][Results]

Therefore, combining the electron and hadronic final state measurements will provide precise determination of basic kinematic variable x, y and Q^2 in the whole kinematic space.

Studies which include QED radiative effects and full GEANT simulation with detailed detector description, and to what precision different unfolding techniques are capable to correct smearing effects are ongoing.

3.3.3 Effect of better resolution barrel EMCal

As was discussed above, high resolution tracking system compensates at large extent the limitations due to moderate resolution of sPHENIX barrel EMCal, for both electron ID and kinematic variables reconstruction. In Fig. 3.21 and 3.22 we study how the improved barrel EMCal resolution, from $\sigma_E/E = 16\%/\sqrt{E} \oplus 5\%$ to $\sigma_E/E = 10\%/\sqrt{E} \oplus 1\%$, would improve electron ID and decrease the smearing effect. The improvement is modest, emphasizing the role of the high resolution tracking system in barrel region.
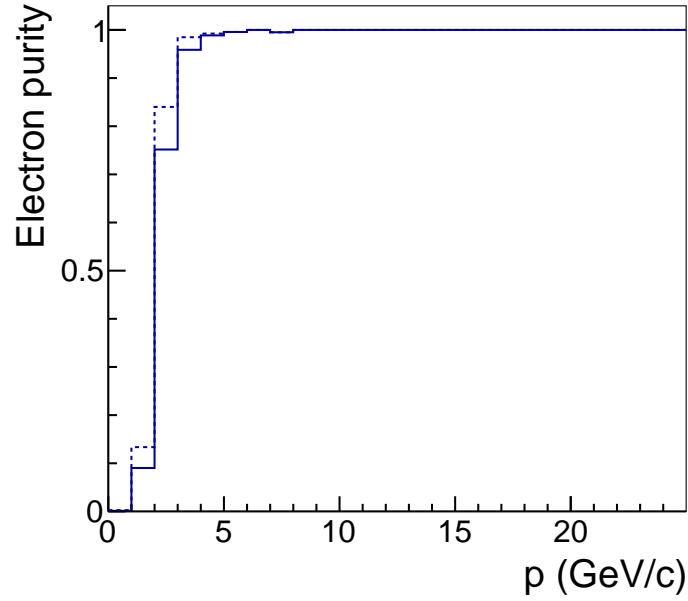
Figure 3.21: For 18 GeV × 275 GeV beam energy configuration, barrel region: The fraction of charged particles from DIS electrons after identification with the EM-Cal+Tracking, for the barrel EMCal resolution $\sigma_E/E = 16\%/\sqrt{E} \oplus 5\%$ (solid) and $\sigma_E/E = 10\%/\sqrt{E} \oplus 1\%$ (dotted).
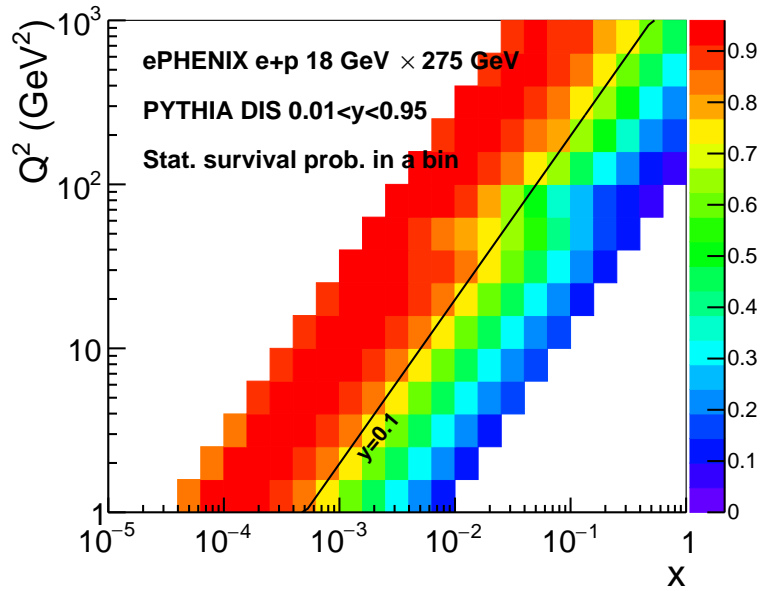

Figure 3.22: The same as Fig. 3.18 but assuming the improved barrel EMCal resolution (see the text).
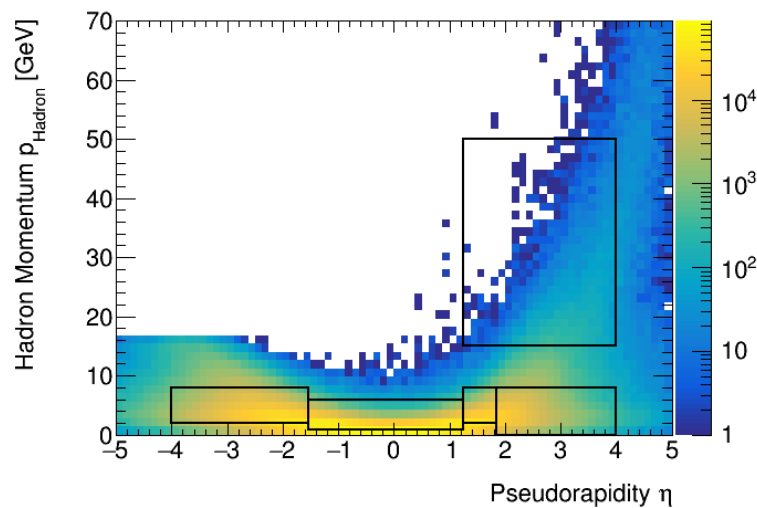
Figure 3.23: Momentum and pseudorapidity distribution for produced hadrons in 20×250 GeV collisions, for hadrons with $z > 0.2$. The boxed regions illustrate the ranges for kaon identification.

3.4 Particle ID Coverage and Performance

The technology options for particle identification are described in Chapter **??**. Table **??** summarizes the pseudorapidity and momentum ranges for a 3-sigma separation of pions and kaons. Figure 3.23 shows the momentum and pseudorapidity ranges for Kaon ID among the final state hadrons with the proposed configuration of PID detectors.

Table 3.2: Momentum and pseudorapidity coverage

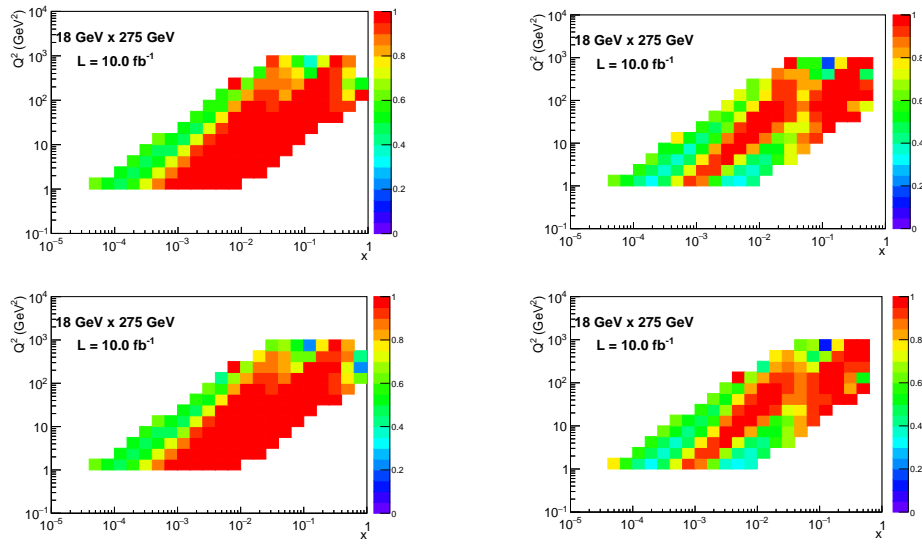| Detector	pseudorapidity	K/π 3σ separation (GeV/c)	e/π 3σ separation (GeV/c)
DIRC	(-1.24, 1.24)	$\sim$6	
dRICH	(1.24, 3.95)	(3,50)	$\sim$3
gas RICH	(1.24, 3.95)	(15,50)	(5, 15)
h-side mRICH	(1.10, 1.85)	(3,9)	$\sim$1.5
e-side mRICH	(-3.9, -1.4)	(3,9)	$\sim$1.5

Figure 3.24: x-Q^2 distributions for the fractions of π^- (top left), π^+ (bottom left), K^- (top right), and K^+ (bottom right) identified with EIC-sPHENIX PID detectors. In all four plots, the z axis is the ratio of particles identified by the PID parameterization in the EIC-sPHENIX smearing simulation to the total number of Monte Carlo particles in a particular $x - Q^2$ bin.

3.5 Charm Tagging

Charm tagging is important for several goals of the EIC physics program. Access to the gluon PDF in both the proton and in nuclei, as well as the gluon single-spin asymmetry arising from the Sivers effect, relies on tagging the photon-gluon fusion process in e-p and e-A collisions [15, 16]. In photon-gluon fusion, a radiated photon from the incident electron interacts with a gluon from the proton or nucleus to create a quark-antiquark pair. Identifying the pair production of a charm and anti-charm quark serves as a more sensitive method of tagging the photon-gluon fusion process, as pair production of up, down and strange quarks are abundant in DIS events. The fragmentation of the pair-produced charm and anti-charm quarks to open charm observables provides one method of tagging the photon-gluon fusion process.

Reconstructing exclusive decays of charmed hadrons is a frequently used method of tagging open charm observables. The D^0 meson, which decays to a pion and kaon pair with a branching ratio of 3.89 ± 0.04 % [17], has already been studied as an open charm observable to tag the photon-gluon fusion process [15, 16]. We have performed simulations to determine the expected D^0 signal that EIC-sPHENIX could detect from reconstructing exclusive D^0 decays to pion and kaon pairs.

Ten million Pythia eRHIC events were generated at the highest beam energy configuration, 18 x 275 GeV, for a variety of DIS processes, including photon-gluon fusion. Events were generated with event kinematics $1 < Q^2 < 1000 \, \text{GeV}^2$, $0.01 < y < 0.95$, and $10^{-5} < x < 0.99$. To simulate realistic detector effects on the determination of particle momenta and PID, the Pythia eRHIC events were run through a simulation of the EIC-sPHENIX detector using the eic-smear detector smearing package. The detector parameterization included current estimates of uncertainties in the energy resolution and PID efficiencies determined from GEANT-4 EIC-sPHENIX studies. Uncertainties in the tracking resolution were estimated from EIC-sPHENIX tracking parameterizations described in Section 3.1. PID parameterization included all PID detectors listed in Table 3.2. The smearing simulation identified pions and kaons only if their momentum and pseudorapidity fell within the ranges of one of the PID detectors. Since the smearing package does not permit particles to fall within the same pseudorapidity and momentum range of multiple PID detectors, the h-side mRICH was truncated to $1.10 < \eta < 1.24$ in the simulation to avoid overlap with the dRICH. Similarly, the gas RICH was not implemented for $\pi - K$ identification in the smearing simulation since the dRICH covers a larger momentum range for $\pi - K$ discrimination over the same pseudorapidity range. Detailed parameterization of PID efficiencies was implemented for the h-side mRICH detector for particles with angle $\theta = 4.8$ - 5.2 ° from the beam axis, while the parameterizations for the other PID detectors were determined according to the momentum ranges listed in Table 3.2 for which the $\pi - K$ and $e - \pi$ separation is at least 3σ.

Figure 3.25 shows the momentum vs. pseudorapidity distribution of pions decayed from D^0 mesons obtained from 10 million Pythia eRHIC events at a beam energy configuration of 18 x 275 GeV. Kaons decayed from D^0 mesons have a similar distribution. Due to most of the pions and kaons from D^0 decays being at central and forward rapidities, the DIRC, dRICH, and mRICH detectors provide critical hadron identification necessary to detect D^0 decays. Only pions and kaons identified by EIC-sPHENIX PID detectors, with pseudorapidity $-2.5 < \eta < 2.5$, and with transverse momentum p_T greater than 0.1 GeV/c
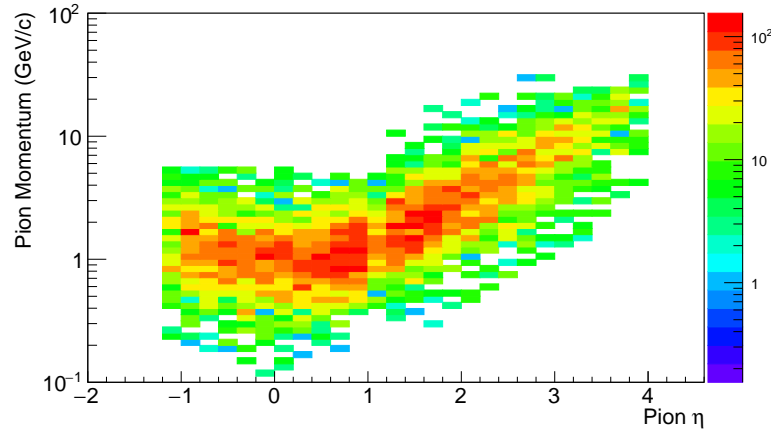
Figure 3.25: Momentum vs pseudorapidity distribution for pions decayed from D^0 mesons produced in the 18 x 275 GeV beam energy configuration from 10 million Pythia eRHIC events.

were used to calculate the invariant mass spectrum of $\pi - K$ pairs from the 10 million smeared Pythia eRHIC events. The pseudorapidity cut was implemented to correspond to the range over which EIC-sPHENIX tracking parameterizations were available. As seen in Figure 3.25, the range $-2.5 < \eta < 2.5$ covers the majority of pions produced from D^0 decays. To reduce the large uncertainties in the smeared particle energies, the energies of identified pions and kaons were re-calculated using the smeared momenta and known particle masses. Figure 3.26 shows the D^0 mass peak reconstructed from smeared pions and kaons. A peak near the D^0 mass at approximately 1.865 GeV is clearly distinguished above the fit to the combinatorial background. The fit estimates an expected yield of approximately 775,000 D^0 mesons detected by EIC-sPHENIX in one year of EIC operation.
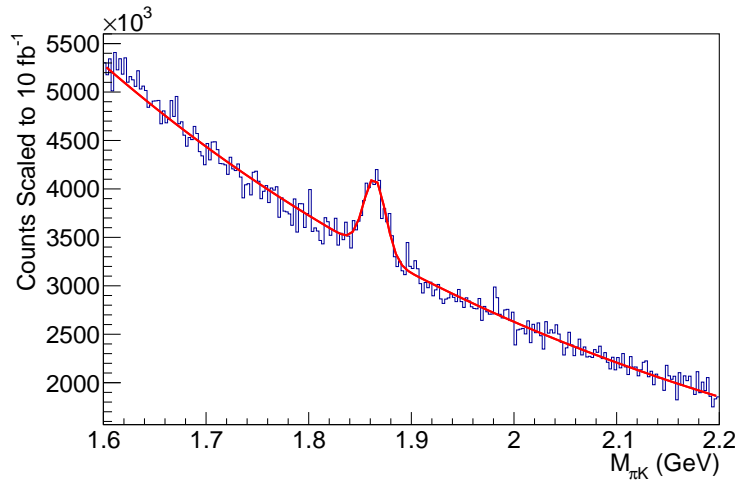
Figure 3.26: A fit to the D^0 mass peak from reconstruction of the exclusive decay $D^0 \to K^-\pi^+$ using smeared Pythia eRHIC events

3.6 DVCS Reconstruction

Deeply Virtual Compton Scattering (DVCS) events provide a potent technique for imaging the spatial distribution of partons inside the proton because they leave it intact, interacting with its constituents only through exchange of a virtual photon. This is of considerable interest since investigating angular momentum contributions to the proton's spin requires an understanding of its three-dimensional structure. In this section, we discuss the ability of an EIC detector at sPHENIX to measure DVCS events.

The primary consideration for DVCS events is the ability to reliably capture all three of the final particles (electron, proton, photon). At all four representative EIC energies (5×100 GeV, 10×100 GeV, 10×275 GeV, and 18×275 GeV), a pseudorapidity coverage of $-4 < \eta < 4$ in the detector was (based purely on geometry) sufficient to capture the electron and proton in over 98% of events we (S. Fazio) simulated with the DVCS-specialized event generator MILOU. These events used kinematic cuts of $1 < Q2 < 100$ GeV^2, $10^-4 < x < 0.5$, $0.01 < y < 0.95$, and $0.01 < |t| < 1.4$ GeV^2. Figure 3.27 shows the energy distribution of photons produced, most of which travel in the electron-going direction (negative η).

Distinguishing proton and electron events is straightforward, as they exit on opposite sides of the beam pipe; running MILOU events through GEANT 4 shows the clusters are separated azimuthally by between 90 and 180 degrees for Mandelstam $t < 1$ GeV^2, making them easily distinguishable. See Figure 3.28.

Capturing the proton is more difficult, as it exits at a very forward pseudorapidity (> 5), necessitating the inclusion of a Roman Pot detector if all three products are to be measured. As discussed in Section 2.5 the resolution of our t reconstruction will depend heavily on the Roman Pots resolution as well as the in-flight magnetic distortion of the protons' trajectories as they approach the Roman Pots stations. Assuming the use of "parallel to point focusing" where protons at small angles are focused after leaving the main detector in order to further distinguish the exclusive DIS protons from other high η products, the original scattering angle can be reconstructed through the application of a 4-by-4 transport matrix.

$$M = \begin{pmatrix} a_{11} & L_x^{eff} & a_{13} & a_{14} \\ a_{21} & a_{22} & a_{23} & a_{24} \\ a_{31} & a_{32} & a_{33} & L_y^{eff} \\ a_{41} & a_{42} & a_{43} & a_{44} \end{pmatrix} \longrightarrow \begin{pmatrix} x^{RP} \\ \theta_x^{RP} \\ y^{RP} \\ \theta_y \end{pmatrix} = M * \begin{pmatrix} x \\ \theta_x \\ y \\ \theta_y \end{pmatrix}$$

The variables labeled RP are observables detected by the Roman Pots while the other values are characteristics of the proton at the point of interaction. x and y correspond to the transverse position of a proton with respect to the beam while $\theta_x = \theta * \sin(\phi)$ and $\theta_y = \theta * cos(\phi)$ take the the proton scattering angle (θ) as well as the azimuthal orientation of the protons (ϕ) into account. The parallel to point focusing minimizes the contribution of the transverse displacement of the protons at the IP, making the effective lengths of the focusing (L_x^{eff} and L_y^{eff}) the leading terms in M while the a_{ij} terms become negligible.
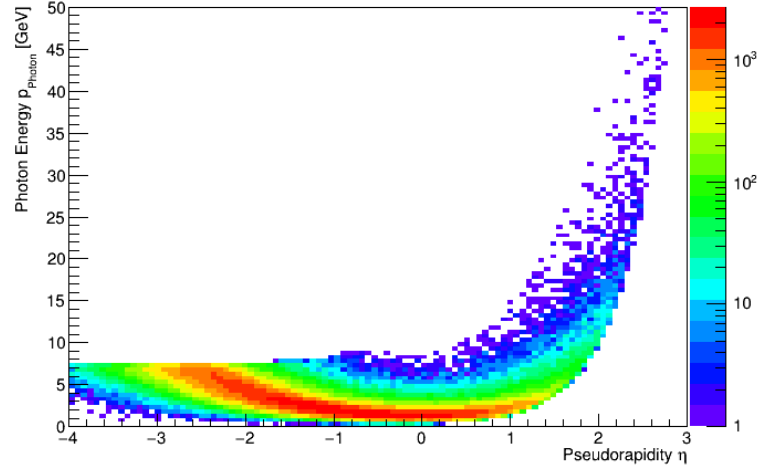
Figure 3.27: For the 18×275 GeV beam energy configuration, DVCS photon energy vs. pseudorapidity distribution; the z-axis scale shows the relative distribution of events from the MILOU event generator.

$$x^{RP} = a_{11}x + L_x^{eff}\theta_x + a_{13}y + a_{14}\theta_y \approx L_x^{eff} * \theta_x$$
$$y^{RP} = a_{31}x + a_{32}\theta_x + a_{33}y + L_y^{eff}\theta_y \approx L_t^{eff} * \theta_y$$

1   The reconstruction technique for this study of t-resolution is $t = 2 * p^2 * (1 - \cos\theta)$,
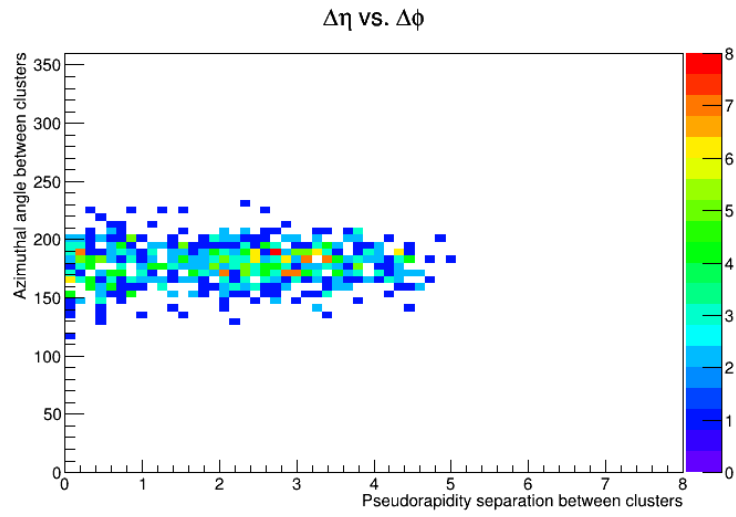2   where p is the proton momentum going into the interaction.

Figure 3.28: Separation in azimuthal angle and pseudorapidity of electron-photon cluster pairs, after running 1,000 MILOU events through GEANT 4 at a beam energy of 18×275 GeV.

3.7 J/ψ Reconstruction

One of the ways of demonstrating the capabilities of the EIC detector system is by reconstructing the invariant mass of a J/ψ. Specifically, J/ψ produced by Deeply Virtual Meson Production (DVMP) serve as an essential tool for probing quarks and gluons of protons. This provides spatial imaging of these partons and their contribution to the total proton spin. This section discusses the DVMP event process and the effectivness of an EIC detector in reconstructing the J/ψ's invariant mass.

During the DVMP process, a vector meson is produced which quickly decays into a variety of decay modes. The primary decay mode of the J/ψ is hadronic, however it is of interest to reconstruct the J/ψ through its rarer e^-e^+ decay. For accurate reconstruction, the momentum vectors of the decay products must be recovered. The charged particle decay selected allows for tracking by the TPC and planar GEM detectors in the h-going and e-going directions. To seperate these lepton decay candidates from other charged hadronic tracks, energy over momentum (E/p) cuts using the barrel and endcap calorimetry are used. Once an electron and positron pair are identified, a formula involving each particle's momentum, psuedorapidity, and polar angle is used to calculate their parent particle's, the J/ψ's, invariant mass.

By using SARTRE, a DVCS and DVMP event generator, an electron and proton were fired at 20x250 GeV collision energy, with an event $Q^2 > 1\text{GeV}^2$ cut. The SARTRE configuration file was set to generate specifically virtual J/ψ which decay into e^-e^+. The event generation data was passed through the Fun4All framework and passed directly to a full detector simulation in GEANT4.
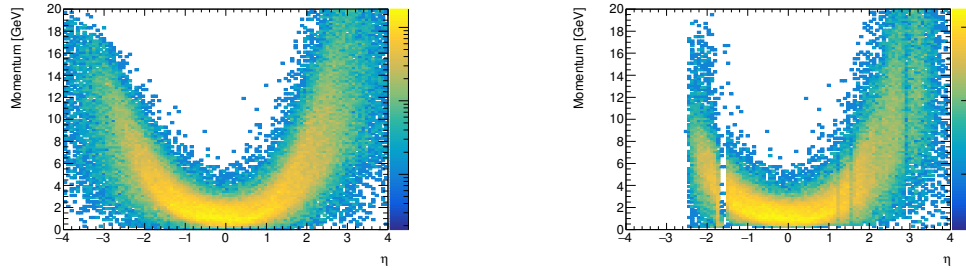

Figure 3.29: Momentum vs. Pseudorapidity distribution of the true decay electron (left) and reconstructed decay electron (right)

The left plots of figures 3.29 and 3.30 are generated using SARTRE simulated collisions, stored within a HepMCEvent. The right plots of these figures are generated by first tagging a reconstructed particle in an event as a scattered electron (using truth information) and then categorizing the remaining reconstructed particles as decay electron or positron based on their track's bending. The cutoff at $\eta > \approx -2.5$ is a feature of the analysis and reconstruction code that is still being investigated. Due to poor momentum reconstruction in the e-going region, the high efficiency of the e-going electromagnetic calorimeter is utilized to substitute particle momentum with cluster energy.

In order to identify leptons, a matching of each calorimeter energy cluster in an event to a particle track is attempted. Depending on the detector and location of the cluster, the track objects reconstructed in each event are extrapolated through the magnetic field to a
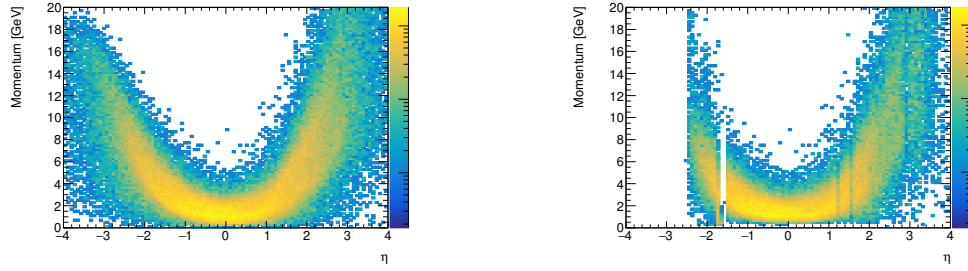
Figure 3.30: Momentum vs. Pseudorapidity distribution of the true decay positron (left) and reconstructed decay positron (right)

1   plane perpendicular to the cluster. Currently, extrapolation of tracks to within 20cm of a
2   cluster 'match' that track to the cluster. This step is crucial for using E/p cuts to isolate
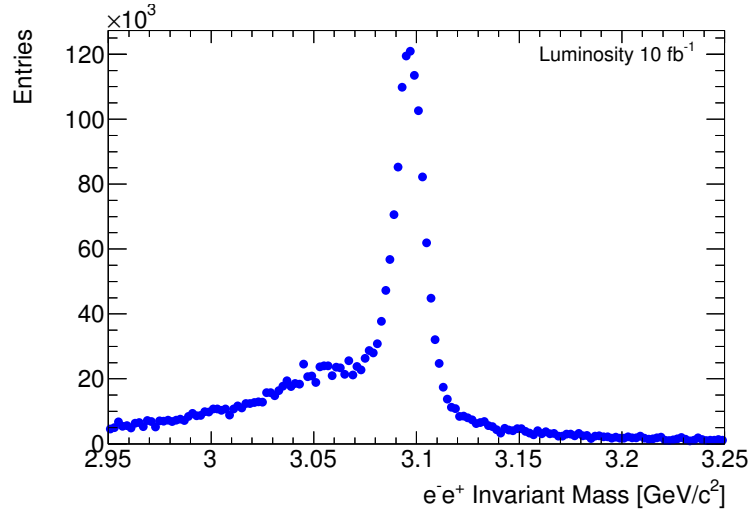3   leptons.

Figure 3.31: *J/ψ*Invariant mass reconstruction distribution using all reconstructed e^-e^+ pairs per event

4   As mentioned previously, the absence of missing reconstructed tracks at pseudorapidi-
5   ties smaller than $\eta = -2.5$ is a feature of the analysis and reconstruction code that is still
6   being investigated. With a large fraction of scattered electrons entering this region, the
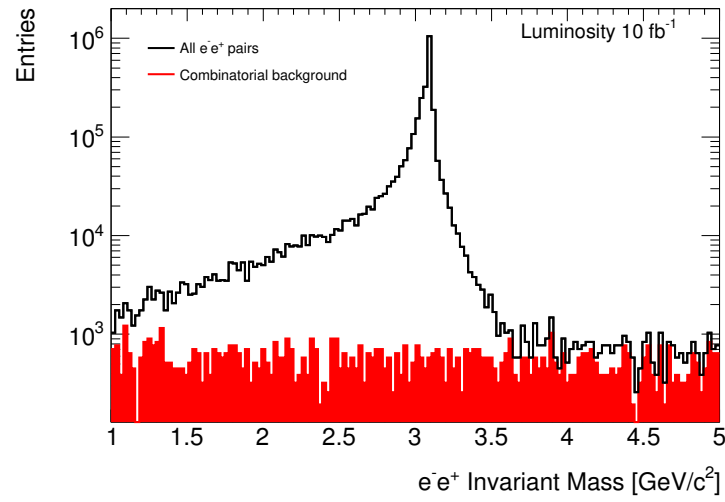7   combinatorial background of Figure 3.32 is underestimated.

Figure 3.32: Comparison of J/ψ Invariant mass reconstruction using all e^-e^+ pairs and pairs which include specifically the scattered electron

4. Conclusion

Bibliography

[1] A. Adare et al. Concept for an Electron Ion Collider (EIC) detector built around the BaBar solenoid. 2014.

[2] A. Accardi et al. Electron Ion Collider: The Next QCD Frontier. *Eur. Phys. J.*, A52 (9):268, 2016. doi: 10.1140/epja/i2016-16268-9.

[3] Daniel Boer et al. Gluons and the quark sea at high energies: Distributions, polarization, tomography. 2011.

[4] BNL. eRHIC Pre-CDR.

[5] B. D. Leverington et al. Performance of the prototype module of the GlueX electromagnetic barrel calorimeter. *Nucl. Instrum. Meth.*, A596:327–337, 2008. doi: 10.1016/j.nima.2008.08.137.

[6] S. A. Sedykh et al. Electromagnetic calorimeters for the BNL muon (g-2) experiment. *Nucl. Instrum. Meth.*, A455:346–360, 2000. doi: 10.1016/S0168-9002(00)00576-3.

[7] C. A. Aidala et al. Design and Beam Test Results for the sPHENIX Electromagnetic and Hadronic Calorimeter Prototypes. *Submitted to: IEEE Trans. Nucl. Sci.*, 2017.

[8] J. D. Osborn and J. Huang. T1044-2017 sPHENIX Test Beam EMCal Analysis. https://indico.bnl.gov/conferenceDisplay.py?confId=3854, 2017.

[9] Engineering National Academies of Sciences and Medicine. *An Assessment of U.S.-Based Electron-Ion Collider Science*. The National Academies Press, Washington, DC, 2018. ISBN 978-0-309-47856-4. doi: 10.17226/25171. URL https://www.nap.edu/catalog/25171/an-assessment-of-us-based-electron-ion-collider-science.

[10] sPHENIX Conceptual Design Report. 2018.

[11] EIC Background Studies and the Impact on the IR and Detector. 2018. URL `https://wiki.bnl.gov/conferences/images/d/d4/ERD21-Report-06272018-Latifa.pdf`.

[12] J. Anderson et al. FELIX: a PCIe based high-throughput approach for interfacing front-end and trigger electronics in the ATLAS Upgrade framework. *JINST*, 11(12): C12023, 2016. doi: 10.1088/1748-0221/11/12/C12023.

[13] J. P. Cachemiche, P. Y. Duval, F. Hachon, R. Le Gac, and F. Réthoré. The PCIe-based readout system for the LHCb experiment. *JINST*, 11(02):P02013, 2016. doi: 10.1088/1748-0221/11/02/P02013.

[14] J. Mitra, S. A. Khan, S. Mukherjee, and R. Paul. Common Readout Unit (CRU) - A new readout architecture for the ALICE experiment. *JINST*, 11(03):C03021, 2016. doi: 10.1088/1748-0221/11/03/C03021.

[15] L. Zheng et al. Accessing the Gluon Sivers Function at a Future Electron-Ion Collider. *Phys.Rev.D*, 98:034011, 2018. doi: 10.1103/PhysRevD.98.034011.

[16] E. Aschenauer et al. Nuclear Structure Functions at a Future Electron-Ion Collier. *Phys.Rev.D*, 96:114005, 2017. doi: 10.1103/PhysRevD.96.114005.

[17] M. Tanabashi and others (Particle Data Group). The Review of Particle Physics (2018). *Phys.Rev.D*, 98:030001, 2018. doi: 10.1103/PhysRevD.98.03001.